Measurement of GMPT Coefficients for Improved Object Characterisation in Metal Detection

T. Özdeğer, P. D. Ledger, W. R. B. Lionheart, J. L. Davidson, and A. J. Peyton

***Abstract*—Magnetic polarizability tensors (MPTs) have become popular for characterising conducting permeable objects and assisting with the identification of hidden objects in metal detection for applications in security screening, humanitarian demining and scrap sorting. A rigorous mathematical justification of the complex symmetric rank 2 MPT object characterisation has been established based on the leading order term in an asymptotic expansion of the perturbed field for small objects. However, the accuracy of an MPT object characterisation is limited by the tensor's small number of independent coefficients. By considering higher order terms in the asymptotic expansion, generalised magnetic polarizabilty tensors (GMPTs) have been introduced and the purpose of this work is to show that GMPT coefficients can, for the first time, be measured in practice. GMPTs offer the possibility to better discriminate between objects and, hence, the potential for better classification and identification, overcoming the limitations of a rank 2 MPT object characterisation. In a metal detector, the low-frequency background fields generated by a set of coils is almost always non-uniform and using GMPTs allow us to make a virtue of this. In this work we include both measurements and simulations to demonstrate the advantages that using GMPTs offer over using an MPT characterisation alone.**

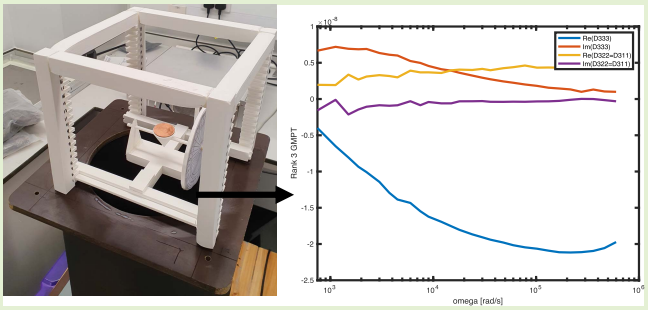

***Index Terms*—Electromagnetic induction spectroscopy, magnetic polarizability tensor, metal detection, metal classification.**

I. Introduction

MAGNETIC polarizability tensors (MPTs) have become popular for characterising conducting permeable objects and assisting with the identification of hidden objects in metal detection for applications in security screening, humanitarian demining and scrap sorting e.g. [1], [2], [9]–[11], [19]–[21], [23], [30]–[32], [35]. A rigorous mathematical theory has been established for the complex symmetric rank 2 MPT characterisation of a small highly conducting permeable isolated object in a non-conducting background. It has been shown that the MPT forms the object description in the leading order term of an asymptotic expansion of the perturbed magnetic field $(\boldsymbol{H}_\alpha - \boldsymbol{H}_0)(\boldsymbol{x})$ as the object size $\alpha \to 0$ [4], [12]. The expansion holds at positions $\boldsymbol{x}$ away from the object. Furthermore, for objects with rotational and reflectional symmetries, it has been established that the number of independent complex coefficients in the MPT can be much smaller than 6 [12]. The leading order term in the asymptotic expansion of $(\boldsymbol{H}_\alpha - \boldsymbol{H}_0)(\boldsymbol{x})$ as $\alpha \to 0$ and an MPT object characterisation has been generalised for multiple and inhomogeneous objects in [16]. Considerable benefits have been seen to be offered by exploiting the spectral behaviour of the MPT coefficients, known as its spectral signature, which provides much richer information than the MPT at a single frequency. This has been understood theoretically [15], efficient algorithms have been developed to compute the MPT spectral signature [33] and these have been applied to compute libraries of MPT spectral signature object characterisations [17]. Machine learning approaches for object classification based on measured and simulated libraries of MPT spectral signatures have also been developed in [19], [20] and [34], respectively.

A complete asymptotic expansion of the perturbed magnetic field $(\boldsymbol{H}_\alpha - \boldsymbol{H}_0)(\boldsymbol{x})$ as $\alpha \to 0$ has been derived in [14],

Manuscript received November 2, 2021; revised November 26, 2021; accepted December 2, 2021. Date of publication December 8, 2021; date of current version January 31, 2022. The work of T. Özdeğer was supported in part by the Engineering and Physical Sciences Research Council (EPSRC) U.K. under the Research Grant EP/R002177 and in part by the Sir Bobby Charlton Foundation. The work of P.D. Ledger was supported by EPSRC under the Research Grant EP/R002134/2, Grant EP/V049453/1, and Grant EP/V009028/1. The work of W. R. B. Lionheart was supported in part by EPSRC under Grant EP/V049496/1 and Grant EP/V009109/1 and in part by the Royal Society through the Royal Society Wolfson Research Merit Award. The associate editor coordinating the review of this article and approving it for publication was Prof. Chao Tan. *(Corresponding author: P. D. Ledger.)*

T. Özdeğer, J. L. Davidson, and A. J. Peyton are with the Department of Electrical and Electronic Engineering, The University of Manchester, Manchester M13 9PL, U.K.

P. D. Ledger is with the School of Computing and Mathematics, Keele University, Staffordshire ST5 5BG, U.K. (e-mail: p.d.ledger@keele.ac.uk).

W. R. B. Lionheart is with the Department of Mathematics, The University of Manchester, Manchester M60 1QD, U.K.

Digital Object Identifier 10.1109/JSEN.2021.3133950

which generalises the earlier results in [4], [12]. In this expansion, new object characterisations called generalised magnetic polarizabilty tensors (GMPTs) have been introduced, building on the MPT object characterisation in the leading order term. The purpose of this work is to show that GMPT coefficients can be measured in practice for the first time. GMPTs offer significant advantages over small object characterisations using the leading order rank 2 MPT descriptions currently used in metal detection. Specifically:

1) Offering the possibility to better discriminate between objects and, hence, offer the potential for better classification and identification, overcoming the limitations of characterising objects using just 6 complex coefficients in a rank 2 MPT description (a simple example of which is to tell which way a cone is pointing).
2) In a metal detector, the low-frequency background fields $\boldsymbol{H}_0$ generated by a set of coils is almost always non-uniform and using GMPTs allow us to make a virtue of this overcoming the assumption that $\boldsymbol{H}_0$ is uniform over the object in a rank 2 description (hence also achieving better 1.).

GMPTs are more complicated than the generalised polarizability tensors (GPT) derived by Ammari and Kang [6] for characterising low conducting inclusions in a scalar electrical impedance tomography (EIT) problem. They have interesting mathematical properties, which we plan to catalogue in a forthcoming work.

The novelties of this work can be summarised as follows: We show, for the first time, that GMPT coefficients and their spectral signature can be obtained in practice from measurements of $(\boldsymbol{H}_\alpha - \boldsymbol{H}_0)(\boldsymbol{x})$ for a multiple coil arrangement using a novel object manipulation device. The resulting measured GMPT spectral signatures we obtain are in good agreement with the simulated GMPT spectral signatures that we calculate from numerical simulations using finite elements. We illustrate that including the GMPT object characterisation information is important to accurately predict $(\boldsymbol{H}_\alpha - \boldsymbol{H}_0)(\boldsymbol{x})$ whenever the background field is non-uniform.

The work is organised as follows: We begin with some notation in Section II. Next, in Section III, we review the complete asymptotic expansion of $(\boldsymbol{H}_\alpha - \boldsymbol{H}_0)(\boldsymbol{x})$ as $\alpha \to 0$ and restrict consideration to terms associated with rank 2 MPT and rank 3 GMPT object characterisations. Then, in Section IV, we apply the asymptotic expansion to a mathematical model of the physical multiple coil arrangement that will be used to generate $\boldsymbol{H}_0$ and to measure $(\boldsymbol{H}_\alpha - \boldsymbol{H}_0)(\boldsymbol{x})$ in the form of a transimpedance measurement. In Section V, we describe how the transimpedance measurements can be used to determine the MPT and GMPT coefficients by rotating the object in a uniform and then non-uniform $\boldsymbol{H}_0$ using an object manipulation device and, in Section VI, we explain how the MPT and GMPT coefficients and their spectral signatures can be predicted numerically. Section VII presents a series of results that compare our measurements and simulations, which demonstrate that GMPT coefficients and their spectral signature can be obtained in practice and that they have an important role to play in predicting $(\boldsymbol{H}_\alpha - \boldsymbol{H}_0)(\boldsymbol{x})$ if $\boldsymbol{H}_0$ is non-uniform. We finish, in Section VIII with some concluding remarks.

II. Notation

We denote by $\boldsymbol{e}_k$ the unit basis vector associated with the kth coordinate direction in a standard orthonormal coordinate system $\boldsymbol{x} = (x_1, x_2, x_3)$ and, hence, the kth component of a vector field $\boldsymbol{v}$ is given by $\boldsymbol{e}_k \cdot \boldsymbol{v} = (\boldsymbol{v})_k = v_k$. We will often use Einstein index summation notation so that a vector can be described as $\boldsymbol{v} = v_k \boldsymbol{e}_k$ and a rank 2 tensor using a calligraphic font as $\mathcal{M} = \mathcal{M}_{kj} \boldsymbol{e}_k \otimes \boldsymbol{e}_j$ where summation is implied over the repeated indices in each case. We will use a Gothic font for higher order tensors so that a rank 3 can be described as $\mathfrak{D} = \mathfrak{D}_{ijk} \boldsymbol{e}_i \otimes \boldsymbol{e}_j \otimes \boldsymbol{e}_k$. The imaginary unit is defined as $\mathrm{i} := \sqrt{-1}$ and we will also use the notation $\|u\|_{L^2(\theta)} := \left(\int_0^{2\pi} |u(\theta)|^2 \mathrm{d}\theta\right)^{1/2}$ to denote the L^2 norm of u over the angles $0 \le \theta \le 2\pi$.

III. Complete Asymptotic Expansion

In [14] Ledger and Lionheart proved the result stated in Theorem 1 below, for describing the magnetic field perturbation $(\boldsymbol{H}_\alpha - \boldsymbol{H}_0)(\boldsymbol{x})$ at a position $\boldsymbol{x}$ due to the presence of a highly conducting object B_α with conductivity σ_* and permeability μ_* in a non-conducting background with conductivity $\sigma = 0$ and the permeability of free space μ_0. The result is applicable away from the object when the eddy current approximation of Maxwell's equations applies [3], which means the excited angular frequency $\omega = 2\pi f$ (with f measured in Hz) of the background field $\boldsymbol{H}_0$ is low and σ_* is high. Additionally, the topology of the object B_α and its size α limits the applicability of the eddy current model, with the eddy current model breaking down for a horse shoe shaped conductor at lower frequencies compared to a solid object of the same size due to capacitive coupling effects [26]. The description $B_\alpha := \alpha B + z$ means that the object can be described by a non-dimensional object B placed at the origin, scaled by a size parameter α and translated by z.

Theorem 1: The magnetic field perturbation in the presence of a small conducting object $B_\alpha = \alpha B + z$ for the eddy current model when $\nu := \omega \sigma_* \mu_0 \alpha^2$ is order one and $\boldsymbol{x}$ is away from the location z of the inclusion is completely described by the asymptotic formula

$$
\begin{aligned}
(\boldsymbol{H}_\alpha - \boldsymbol{H}_0)(\boldsymbol{x})_i \;=\; & \sum_{m=0}^{M-1} \sum_{p=0}^{M-1-m} (\boldsymbol{D}_x^{2+m} G(\boldsymbol{x}, z))_{[i,K(m+1)]} \\
& \mathfrak{M}_{K(m+1)J(p+1)} (\boldsymbol{D}_z^p (\boldsymbol{H}_0(z)))_{J(p+1)} \\
& + (\boldsymbol{R}(\boldsymbol{x}))_i, \qquad (1) \\
J(p+1) := & [j, J(p)] = [j, j_1, j_2, \cdots, j_p], \\
K(m+1) := & [k, K(m)] = [k, k_1, k_2, \cdots, k_m],
\end{aligned}
$$

with $|\boldsymbol{R}(\boldsymbol{x})| \le C\alpha^{3+M} \|\boldsymbol{H}_0\|_{W^{M+1,\infty}(B_\alpha)}$, $G(\boldsymbol{x}, z) := 1/(4\pi|\boldsymbol{x} - z|)$. In the above, $J(p)$ and $K(m)$ are p– and m–tuples of integers, respectively, with each index taking values $1, 2, 3$, and Einstein index summation is implied over

$K(m+1)$ and $J(p+1)$. Also

$$(\boldsymbol{D}_x^{2+m} G(\boldsymbol{x},z))_{[i,K(m+1)]} = \left(\prod_{\ell=1}^{m} \partial_{x_{k_\ell}}\right)(\partial_{x_k}(\partial_{x_i}(G(\boldsymbol{x},z)))),$$

$$(\boldsymbol{D}_z^{p}(\boldsymbol{H}_0(z)))_{J(p+1)} = \left(\prod_{\ell=1}^{p} \partial_{z_{j_\ell}}\right)(\boldsymbol{H}_0(z)\cdot \boldsymbol{e}_j),$$

and the coefficients of a rank $2+p+m$ generalised magnetic polarizability tensor (GMPT) are defined by

$$\mathfrak{M}_{K(m+1)J(p+1)} := -\mathfrak{C}_{K(m+1)J(p+1)} + \mathfrak{N}_{K(m+1)J(p+1)}, \quad (2)$$

where

$$\mathfrak{C}_{K(m+1)J(p+1)} := -\frac{\mathrm{i}\nu\alpha^{3+m+p}(-1)^m}{2(m+1)!p!(p+2)}\boldsymbol{e}_k \cdot \int_B \boldsymbol{\xi}\times\left((\Pi(\boldsymbol{\xi}))_{K(m)}(\boldsymbol{\theta}_{J(p+1)} + (\Pi(\boldsymbol{\xi}))_{J(p)}\boldsymbol{e}_j\times\boldsymbol{\xi})\right)\mathrm{d}\boldsymbol{\xi}, \quad (3a)$$

$$\mathfrak{N}_{K(m+1)J(p+1)} := \left(1-\frac{\mu_0}{\mu_*}\right)\frac{\alpha^{3+m+p}(-1)^m}{p!m!}\boldsymbol{e}_k \cdot \int_B (\Pi(\boldsymbol{\xi}))_{K(m)}\left(\frac{1}{p+2}\nabla_\xi\times\boldsymbol{\theta}_{J(p+1)} + (\Pi(\boldsymbol{\xi}))_{J(p)}\boldsymbol{e}_j\right)\mathrm{d}\boldsymbol{\xi}. \quad (3b)$$

In the above, $\boldsymbol{\theta}_{J(p+1)}$ satisfy the transmission problem

$$\nabla_\xi\times\mu_*^{-1}\nabla_\xi\times\boldsymbol{\theta}_{J(p+1)} - \mathrm{i}\omega\sigma_*\alpha^2\boldsymbol{\theta}_{J(p+1)} - \mathrm{i}\omega\sigma_*\alpha^2(\Pi(\boldsymbol{\xi}))_{J(p)}\boldsymbol{e}_j\times\boldsymbol{\xi} = \boldsymbol{0} \ \text{ in } B\,, \quad (4a)$$

$$\nabla_\xi\cdot\boldsymbol{\theta}_{J(p+1)} = 0 \ \text{ in } \mathbb{R}^3\setminus B \quad (4b)$$

$$\nabla_\xi\times\mu_0^{-1}\nabla_\xi\times\boldsymbol{\theta}_{J(p+1)} = \boldsymbol{0} \ \text{ in } \mathbb{R}^3\setminus B\,, \quad (4c)$$

$$[\boldsymbol{n}\times\boldsymbol{\theta}_{J(p+1)}]_\Gamma = \boldsymbol{0} \text{ on } \Gamma := \partial B, \quad (4d)$$

$$[\boldsymbol{n}\times\mu^{-1}\nabla_\xi\times\boldsymbol{\theta}_{J(p+1)}]_\Gamma = -(p+2)[\mu^{-1}]_\Gamma \cdot(\boldsymbol{n}\times\boldsymbol{e}_j(\Pi(\boldsymbol{\xi}))_{J(p)}) \ \text{ on } \Gamma, \quad (4e)$$

$$\int_\Gamma \boldsymbol{n}\cdot\boldsymbol{\theta}_{J(p+1)}\mathrm{d}\boldsymbol{\xi} = 0, \quad (4f)$$

$$\boldsymbol{\theta}_{J(p+1)} = O(|\boldsymbol{\xi}|^{-1}) \ \text{ as } |\boldsymbol{\xi}|\to\infty\,, \quad (4g)$$

$(\Pi(\boldsymbol{\xi}))_{J(p)} := \prod_{\ell=1}^{p}\xi_{j_\ell} = \xi_{j_1}\xi_{j_2}\cdots\xi_{j_p}$ and in the case $J(p) = \emptyset$ then $(\Pi(\boldsymbol{\xi}))_{J(p)} = 1$.

Note that, compared to [14], we have chosen to simplify the notation so that $\breve{\mathfrak{C}}$ is now written as $\mathfrak{C}$ and $\breve{\breve{\mathfrak{M}}}$ as $\mathfrak{M}$. Furthermore, in this work, we will restrict consideration to objects with $\mu_* = \mu_0$ so that $\mathfrak{N}_{K(m+1)J(p+1)} = 0$ and consider the case of $M = 2$. This means the asymptotic expansion we will consider includes the terms

$$(\boldsymbol{H}_\alpha - \boldsymbol{H}_0)(\boldsymbol{x})_i = (\boldsymbol{D}_x^2 G(\boldsymbol{x},z))_{ik}\mathcal{M}_{kj}(\boldsymbol{H}_0(z)))_j + \frac{1}{8}(\boldsymbol{D}_x^3 G(\boldsymbol{x},z))_{ikk_1}\mathfrak{D}_{kk_1j}(\boldsymbol{H}_0(z))_j - \frac{1}{6}(\boldsymbol{D}_x^2 G(\boldsymbol{x},z))_{ik}\mathfrak{D}_{kjj_1}(\boldsymbol{D}_z(\boldsymbol{H}_0(z)))_{jj_1} + (\boldsymbol{R}(\boldsymbol{x}))_i, \quad (5)$$

with $|\boldsymbol{R}(\boldsymbol{x})| \le C\alpha^5\|\boldsymbol{H}_0\|_{W^{3,\infty}(B_\alpha)}$ describing the behaviour of the residual. In the above, the coefficients $\mathcal{M}_{kj} \equiv \mathfrak{M}_{kj}$ are associated with a complex symmetric rank 2 MPT characterisation $\mathcal{M} = \mathcal{M}_{kj}\boldsymbol{e}_k\otimes\boldsymbol{e}_j$, which follows since $\mathfrak{M}_{kj}$ reduces to the rank 2 MPT coefficients $\mathcal{M}_{kj}$ previously considered in [12], [13], [15], [16] where it has been shown that $\mathcal{M}_{kj} = \mathcal{M}_{jk}$. The coefficients $\mathfrak{D}_{kk_1j}$ and $\mathfrak{D}_{kjj_1}$ are associated with scaled rank 3 GMPT characterisations

$$\mathfrak{D} = \mathfrak{D}_{kk_1j}\boldsymbol{e}_k\otimes\boldsymbol{e}_{k_1}\otimes\boldsymbol{e}_j, \quad \mathfrak{D} = \mathfrak{D}_{kjj_1}\boldsymbol{e}_k\otimes\boldsymbol{e}_j\otimes\boldsymbol{e}_{j_1}, \quad (6)$$

where

$$\mathfrak{D}_{K(m+1)J(p+1)} := (-1)^m 2(m+1)!p!(p+2)\mathfrak{C}_{K(m+1)J(p+1)}. \quad (7)$$

Furthermore, for $\mu_* = \mu_0$, the GMPT has the following symmetry

$$\mathfrak{D}_{K(m+1)J(p+1)} = \mathfrak{D}_{J(p+1)K(m+1)}, \quad (8)$$

which does not follow from reciprocity and is somewhat involved to prove. The proof will form part of a forthcoming work on the mathematical properties of GMPTs.

The coefficients $\mathcal{M}_{kj}$ are independent of the choice of origin for $\boldsymbol{\xi}$ [4], [5], [16] and, hence, the MPT object characterisation is independent of the object's position. However, in common with GPTs for the EIT problem [6], the coefficients $\mathfrak{D}_{kk_1j}$ of the scaled rank 3 GMPT depend on the choice of origin for $\boldsymbol{\xi}$. For this work, we choose the origin to be the object's centroid (centre of mass assuming uniform density).

Using $\mathcal{M}$ alone to characterise objects has limitations since, at most, an object is characterised by 6 complex coefficients as a function of ω. However, for objects with rotational and/or reflectional symmetries the number of independent coefficients is much fewer and this makes it difficult to discriminate between objects in object classification and to determine which way an object (such as a cone) is pointing. By additionally using $\mathfrak{D}$ provides up to an additional 11 complex coefficients as a function of ω, which can aid with discriminating between objects when undertaking classification. Although, for objects with mirror and/or reflectional symmetries, the number of independent coefficients of $\mathfrak{D}$ also reduces. In the following we explain how the MPT and GMPT coefficients can be measured and simulated in practice.

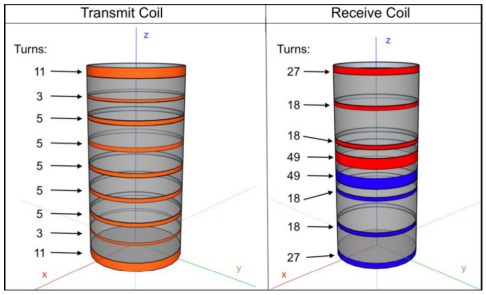

(*a*)

(*b*)

Fig. 1. Configuration of the multiple transmit and receive coil arrangement showing (a) turns in each coil and (b) the actual coil array.

IV. Mathematical Model of the Coil Arrangement

The induced voltage in a coil C with a single clockwise winding, for an object positioned at $\boldsymbol{z}$, can be expressed as

$$\begin{aligned} V^{\text{ind}} &= \int_C (\boldsymbol{E}_\alpha - \boldsymbol{E}_0)(\boldsymbol{x}) \cdot \tau \, \mathrm{d}\boldsymbol{x} \\ &= \int_S \nabla \times (\boldsymbol{E}_\alpha - \boldsymbol{E}_0)(\boldsymbol{x}) \cdot \boldsymbol{n} \mathrm{d}\boldsymbol{x} \\ &= \mathrm{i}\omega\mu_0 \int_S (\boldsymbol{H}_\alpha - \boldsymbol{H}_0)(\boldsymbol{x}) \cdot \boldsymbol{n} \mathrm{d}\boldsymbol{x}, \end{aligned} \tag{9}$$

where $C = \partial S$, $\boldsymbol{\tau}$ is the unit tangent to C and $\boldsymbol{n}$ is the unit normal to S. Upon substitution of (1), the evaluation of V^{ind} reduces to performing integrals of components of $(\boldsymbol{D}_x^{2+m} G(\boldsymbol{x}, \boldsymbol{z}))$ with respect to $\boldsymbol{x}$ over the surface S.

The particular coil configuration considered is shown in Fig. 1 and consists of 8 receive (Rx) coils and 9 transmit (Tx) coils coaxially arranged in a vertical stack so that $\boldsymbol{n} = \boldsymbol{e}_3$ in (9). Coils Rx1-Rx4 are wound in a clockwise orientation while coils Rx5-Rx9 are wound in an anticlockwise orientation. Defining

$$w(n) = \begin{cases} 1 & n = 1, \ldots, 4 \\ -1 & n = 5, \ldots, 8, \end{cases} \tag{10}$$

then the induced voltage is given by the sum

$$V^{\text{ind}} = \mathrm{i}\omega\mu_0 \sum_{n=1}^{8} \frac{w(n) N_{\text{Rx}}(n)}{L_{\text{Rx}}(n)} \int_{S_{\text{Rx}}(n)} (\boldsymbol{H}_\alpha - \boldsymbol{H}_0)(\boldsymbol{x}) \cdot \boldsymbol{e}_3 \mathrm{d}\boldsymbol{x}, \tag{11}$$

where $S_{\text{Rx}}(n)$, $N_{\text{Rx}}(n)$ and $L_{\text{Rx}}(n)$ are the enclosed surface, number of turns and length of the nth Rx coil, respectively. The background field $\boldsymbol{H}_0$ at the position $\boldsymbol{z}$ that is created by the Tx coils can be expressed as the sum

$$\begin{aligned} \boldsymbol{H}_0(\boldsymbol{z}) &= \boldsymbol{H}_0^{\text{Tx}}(\boldsymbol{z}) \\ &= \sum_{n=1}^{9} \boldsymbol{H}_{\text{coil}}(N_{\text{Tx}}(n), I_{\text{Tx}}(n), L_{\text{Tx}}(n), R_{\text{Tx}}(n), \\ &\quad z_1 \boldsymbol{e}_1 + z_2 \boldsymbol{e}_2 + (z_3 - L_{\text{Tx}}(n)/2 - p_{\text{Tx}}(n)) \boldsymbol{e}_3), \end{aligned} \tag{12}$$

where $N_{\text{Tx}}(n)$, $I_{\text{Tx}}(n)$, R_{Tx}, L_{Tx} are the number of turns, current flowing, radius and length of the nth Tx coil, respectively and $p_{\text{Tx}}(n)$ describes the vertical position (base) of the nth Tx coil. In addition, if $\boldsymbol{z} \parallel \boldsymbol{e}_3$, we have the well known form

$$\begin{aligned} &\boldsymbol{H}_{\text{coil}}(N, I, L, R, \boldsymbol{z}) \\ &\quad = \frac{NI}{2L} \left(\frac{\frac{L}{2R} - \frac{z_3}{R}}{\sqrt{1 + \left(\frac{L}{2R} - \frac{z_3}{R}\right)^2}} + \frac{\frac{L}{2R} + \frac{z_3}{R}}{\sqrt{1 + \left(\frac{L}{2R} + \frac{z_3}{R}\right)^2}} \right) \boldsymbol{e}_3, \end{aligned}$$

for the background field on axis resulting from a solenoid. Off-axis, the representation of $\boldsymbol{H}_{\text{coil}}$ is also known analytically [7]. For the coil arrangement considered, the details are provided in Table I so that the overall height of the arrangement is 500 mm. The non-uniformity of the background field $\boldsymbol{H}_0^{\text{Tx}}$ exterior to the coil array is illustrated in the finite element simulation shown in Fig. 2 (*a*), which is in close agreement with the analytical model, as Fig. 2 (*b*) shows.

Furthermore, introducing

$$(\boldsymbol{H}_0^{\text{Rx}}(\boldsymbol{z}))_k := \sum_{n=1}^{8} \frac{w(n) N_{\text{Rx}}(n)}{L_{\text{Rx}}(n)} \int_{S(n)} \boldsymbol{D}_x^2 G(\boldsymbol{x}, \boldsymbol{z})_{3k} \mathrm{d}\boldsymbol{x}, \tag{13}$$

for the background field that would be produced by the Rx coils if excited by a unit current source at position $\boldsymbol{z}$ then it is easy to show that

$$\begin{aligned} &(\boldsymbol{D}_z(\boldsymbol{H}_0^{\text{Rx}})(\boldsymbol{z}))_{kk_1} \\ &\quad := \sum_{n=1}^{8} \frac{w(n) N_{\text{Rx}}(n)}{L_{\text{Rx}}(n)} \int_{S(n)} (\boldsymbol{D}_z(\boldsymbol{D}_x^2 G(\boldsymbol{x}, \boldsymbol{z})))_{3kk_1} \mathrm{d}\boldsymbol{x} \\ &\quad = -\sum_{n=1}^{8} \frac{w(n) N_{\text{Rx}}(n)}{L_{\text{Rx}}(n)} \int_{S(n)} (\boldsymbol{D}_x^3 G(\boldsymbol{x}, \boldsymbol{z}))_{3kk_1} \mathrm{d}\boldsymbol{x}. \end{aligned} \tag{14}$$

By substituting (5) into (11), replacing $\boldsymbol{H}_0(\boldsymbol{z})$ by the expression given in (12) and using (13) and (14), it can be shown that V^{ind} takes the simple form

$$V^{\text{ind}} = V_2^{\text{ind}}(\mathcal{M}) + V_3^{\text{ind}}(\mathfrak{D}) + V_r^{\text{ind}}, \tag{15}$$

where $V_2^{\text{ind}}(\mathcal{M})$ denotes the rank 2 contribution, $V_3^{\text{ind}}(\mathfrak{D})$ denotes the rank 3 contribution and $V_r \leq C\alpha^5 \|\boldsymbol{H}_0\|_{W^{3,\infty}(B_\alpha)}$ denotes the residual, which, as we will see, will be small

TABLE I
PARAMETERS DESCRIBING THE MULTIPLE COIL ARRANGEMENT

$N_{\mathrm{Rx}}(n)$	27	18	18	49	49	18	18	27
$L_{\mathrm{Rx}}(n)$ (mm)	10	4	4	22	22	4	4	10
$p_{\mathrm{Rx}}(n)$ (mm)	234	155	61	14	-36	-65	-159	-244
$R_{\mathrm{Rx}}(n)$ (mm)	220	220	220	220	220	220	220	220

$I_{\mathrm{Tx}}(n)N_{\mathrm{Tx}}(n)$ (A)	3.67	1	1.67	1.67	1.67	1.67	1.67	1	3.67
$L_{\mathrm{Tx}}(n)$ (mm)	23.1	6.3	10.5	10.5	10.5	10.5	10.5	6.3	23.1
$p_{\mathrm{Tx}}(n)$ (mm)	226.9	172.6	119.1	57.25	-5.25	-67.75	-129.6	-178.9	-250
$R_{\mathrm{Tx}}(n)$ (mm)	240	240	240	240	240	240	240	240	240

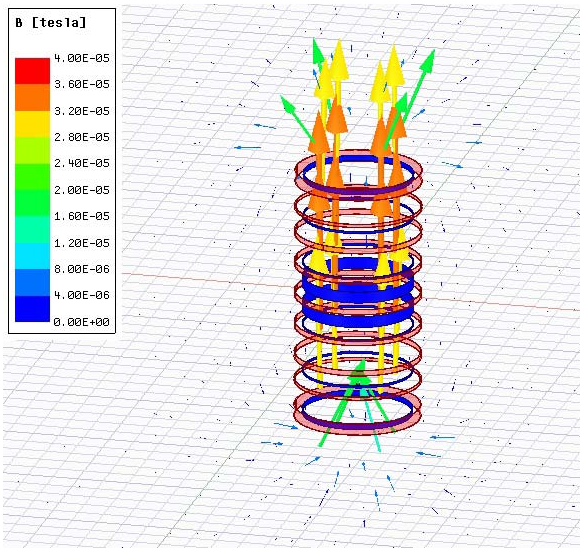

(a)

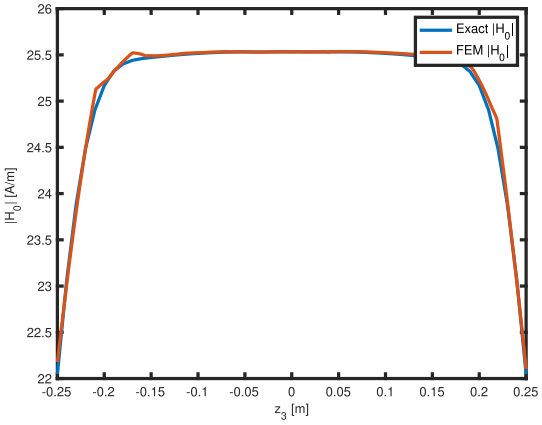

(b)

Fig. 2. Illustration of the background field showing (a) the simulated field lines of $\boldsymbol{B}_0^{\mathrm{Tx}} = \mu_0 \boldsymbol{H}_0^{\mathrm{Tx}}$ around the coil array using a finite element model and (b) $|\boldsymbol{H}_0^{\mathrm{Tx}}(\boldsymbol{z})|$ evaluated for positions $\boldsymbol{z}$ along the axis of the coil array where $\boldsymbol{z} \parallel \boldsymbol{e}_3$ comparing (12) with a finite element model of the coil array.

for the problems we will consider. Explicitly, for the case considered in this work,

$$V_2^{\mathrm{ind}}(\mathcal{M}) := \mathrm{i}\omega\mu_0 (\boldsymbol{H}_0^{\mathrm{Rx}}(z))_i \mathcal{M}_{ij} (\boldsymbol{H}_0^{\mathrm{Tx}}(z))_j \tag{16a}$$

$$\begin{aligned} V_3^{\mathrm{ind}}(\mathfrak{D}) &:= \mathrm{i}\omega\mu_0 \Big(-(\boldsymbol{D}_z(\boldsymbol{H}_0^{\mathrm{Rx}}(z)))_{kk_1} \mathfrak{M}_{kk_1 j} (\boldsymbol{H}_0^{\mathrm{Tx}}(z))_j \\ &\quad + (\boldsymbol{H}_0^{\mathrm{Rx}}(z))_k \mathfrak{M}_{kjj_1} (\boldsymbol{D}_z(\boldsymbol{H}_0^{\mathrm{Tx}}(z)))_{jj_1} \Big) \\ &= \mathrm{i}\omega\mu_0 \Big(-\frac{1}{8} (\boldsymbol{D}_z(\boldsymbol{H}_0^{\mathrm{Rx}}(z)))_{kk_1} \mathfrak{D}_{kk_1 j} (\boldsymbol{H}_0^{\mathrm{Tx}}(z))_j \\ &\quad - \frac{1}{6} (\boldsymbol{H}_0^{\mathrm{Rx}}(z))_k \mathfrak{D}_{kjj_1} (\boldsymbol{D}_z(\boldsymbol{H}_0^{\mathrm{Tx}}(z)))_{jj_1} \Big) \\ &= -\mathrm{i}\omega\mu_0 \mathfrak{D}_{kk_1 j} \Big(\frac{1}{8} (\boldsymbol{D}_z(\boldsymbol{H}_0^{\mathrm{Rx}}(z)))_{kk_1} (\boldsymbol{H}_0^{\mathrm{Tx}}(z))_j \\ &\quad + \frac{1}{6} (\boldsymbol{H}_0^{\mathrm{Rx}}(z))_j (\boldsymbol{D}_z(\boldsymbol{H}_0^{\mathrm{Tx}}(z)))_{kk_1} \Big), \end{aligned} \tag{16b}$$

where $\mu_* = \mu_0$ has been assumed and the symmetry condition (8) has been used in the latter result.

We observe that $V_3^{\mathrm{ind}}(\mathfrak{D})$ provides a natural extension of the familiar $V_2^{\mathrm{ind}}(\mathcal{M})$ term for a rank 3 GMPT object characterisation. For an object placed on axis and in the centre of the coil arrangement, $\boldsymbol{H}_0^{\mathrm{Tx}}(z)$ is near uniform and the contribution V_2^{ind} dominates, while V_3^{ind} is negligible. However, for an object placed outside of the coil arrangement $\boldsymbol{H}_0^{\mathrm{Tx}}(z)$ is non-uniform and $\|\boldsymbol{D}_z(\boldsymbol{H}_0^{\mathrm{Tx}}(z))\|$ can become large. Indeed, if $\boldsymbol{H}_0^{\mathrm{Tx}}(z)$ is strongly non-uniform, $V_3^{\mathrm{ind}}(\mathfrak{D})$ becomes increasingly important and can dominate over $V_2^{\mathrm{ind}}(\mathcal{M})$.

If an object B is rotated by an angle θ about a coordinate axis, its transformation can be described by $B' = \mathbf{R}(\theta)(B)$ where $\mathbf{R}(\theta)$ is an orthogonal rotation matrix. Accordingly, the coefficients of $\mathcal{M}$ and $\mathfrak{D}$ transform as

$$\mathcal{M}'_{ij} = (\mathbf{R})_{ip} (\mathbf{R})_{jq} \mathcal{M}_{pq}, \tag{17a}$$

$$\mathfrak{D}'_{ijk} = (\mathbf{R})_{ip} (\mathbf{R})_{jq} (\mathbf{R})_{kr} \mathfrak{D}_{pqr}. \tag{17b}$$

Then, by replacing $\mathcal{M}_{ij}$ by $\mathcal{M}'_{ij}$ and $\mathfrak{D}_{kk_1 j}$ by $\mathfrak{D}'_{kk_1 j}$ in (16), we obtain $V_2^{\mathrm{ind}}(\mathcal{M}, \theta)$ and $V_3^{\mathrm{ind}}(\mathfrak{D}, \theta)$ for the rank 2 and rank 3 contributions to $V^{\mathrm{ind}}(\theta)$ as a function of object rotation angle.

Throughout, we will normalise the presented results of V^{ind} by $\omega\mathrm{i}$ and we will refer to $\mathrm{Re}(V^{\mathrm{ind}}/(\omega\mathrm{i}))$ as the reactive and $\mathrm{Im}(V^{\mathrm{ind}}/(\omega\mathrm{i}))$ as the resistive components of the transimpedance, respectively.

V. MEASUREMENT OF TENSOR COEFFICIENTS

The procedure for measuring the coefficients of $\mathcal{M}$ and $\mathfrak{D}$ for a given object αB breaks down in to first determining those of $\mathcal{M}$ and then those of $\mathfrak{D}$ for each excitation frequency of interest. We describe each of these steps separately in the following.

A. Measuring the Coefficients of the Rank 2 MPT

If the object's position z is chosen to be along the axis of the coil array, such that $\boldsymbol{z} \parallel \boldsymbol{e}_3$, and if z_3 is chosen within the volume of the coil array, away from its ends, $\boldsymbol{H}_0^{\mathrm{Tx}}(z)$ is near uniform. For the coil array described in Table I, this occurs when -0.155 m $\leq z_3 \leq 0.155$ m, as shown in Fig. 2 (b). Hence, for objects placed in such locations, V_3^{ind} does not

Fig. 3. Target orientation manipulator capable of rotating objects around one axis.

contribute to V^{ind} and the measurements $V^{\text{ind,meas}}(\theta)$ can be used to determine $\mathcal{M}_{ij}$. Noting that $V_2^{\text{ind}}(\mathcal{M},\theta)$ is linear in the coefficients of $\mathcal{M}$, and that these are independent of the object's position, we can determine $\mathcal{M}_{ij}$ as the solution to the least squares problem

$$\min_{\mathcal{M}_{ij}} |g(\theta_n,\mathcal{M})|^2 = \min_{\mathcal{M}_{ij}} \sum_{n=1}^{N_\theta} \left| V^{\text{ind,meas}}(\theta_n) - V_2^{\text{ind}}(\mathcal{M},\theta_n) \right|^2,$$

where N_θ is the total number of angles θ_n considered. This process is repeated for each excitation frequency of interest leading to the object's measured MPT spectral signature Consideration must be given to the number of angles as well as to the number of rotation axes considered [13], [25] to ensure that all the independent coefficients of $\mathcal{M}$ are properly found.

In practice, the above process is achieved by placing the objects at the aforementioned location and by performing rotations using the bespoke target orientation manipulator shown in Fig. 3. Using this apparatus, objects are rotated about different coordinate axes with a fixed degree increment. For each orientation, a frequency sweep between $f_{\min}$ and $f_{\max}$ is performed and V^{ind} for each frequency recorded. The control of system electronics and the data acquisition during the experiments is done automatically.

B. Measuring the Coefficients of $\mathfrak{D}$

Once the coefficients of $\mathcal{M}$ are found, we can then determine the coefficients of $\mathfrak{D}$ by placing the object at a position $\boldsymbol{z}$ where the background field $\boldsymbol{H}_0^{\text{Tx}}(\boldsymbol{z})$ is non-uniform. This is achieved by placing the object on the axis of the coil array with $z_3 > 0.155$ m, performing rotations about different coordinate axes and solving the least squares problem

$$\min_{\mathfrak{D}_{kk_1j}} \sum_{n=1}^{N_\theta} |h(\theta_n,\mathcal{M},\mathfrak{D})|^2 = \min_{\mathfrak{D}_{kk_1j}} \sum_{n=1}^{N_\theta} \left| V^{\text{ind,meas}}(\theta_n) - V_2^{\text{ind}}(\mathcal{M},\theta_n) - V_3^{\text{ind}}(\mathfrak{D},\theta_n) \right|^2, \tag{18}$$

for $\mathfrak{D}_{kk_1j}$ for each frequency of interest leading to the object's measured GMPT spectral signature. Note that $V_3^{\text{ind}}(\mathfrak{D},\theta_n)$ is linear in the unknown $\mathfrak{D}_{kk_1j}$ and that $V_2^{\text{ind}}(\mathcal{M},\theta_n)$ can be evaluated since the coefficients of $\mathcal{M}$ have been found previously and the object position $\boldsymbol{z}$ has been chosen. As in Section V-A, important consideration must be given to N_θ and the choice of θ_n [13].

Given that the object is positioned manually, its position $\boldsymbol{z}$ is only known approximately. If we know that the object is placed on the $\boldsymbol{e}_3$ axis, an improved estimate of its vertical elevation z_3 can be found by solving the minimisation problem

$$\min_{z_3} \sum_{n=1}^{N_\theta} \left| V^{\text{ind,meas}}(\theta_n) - V_2^{\text{ind}}(\mathcal{M},\theta_n,z_3) \right|^2, \tag{19}$$

for the global minimum z_3, where we have emphasised that V_2^{ind} also depends on z_3. Once this improved estimate is found, it can be used in (18) to aid with determining $\mathfrak{D}_{kk_1j}$.

In practice, the above process is achieved by placing objects in the non-uniform part of the field by using the mechanical arrangement in Fig. 4. The same approach of incrementing the rotation by fixed angle increment and sweeping through the frequencies $f_{\min}$ and $f_{\max}$, as described in Section V-A, is performed. However, the apparatus shown in this figure allows the object to be placed in different positions in both vertical and horizontal direction for each experiment. In particular, the apparatus allows the vertical position of an object to be adjusted in 10 mm steps using the slots on the arrangement. The object's horizontal position can be also adjusted in 10 mm steps on both the x_1 and x_2 axes by placing the arrangement into pre-marked positions on the lid of the coil arrangement

VI. Predicting the Tensor Coefficients Using Numerical Simulations

The numerical prediction of the coefficients of $\mathcal{M}$ and $\mathfrak{D}$ for a chosen object αB follows a similar procedure to that described previously for the computation of the coefficients of the rank 2 MPT [12], [13]. This involves approximating the solution $\boldsymbol{\theta}_{J(p+1)}$ to the transmission problem (4) by constructing weak discrete finite element approximations using an $\boldsymbol{H}(\text{curl})$ conforming discretisation, which is appropriate for this problem, where the both mesh spacing h and element order q[1] can be refined in order to improve the accuracy of the numerical solution. The Coulomb gauge $\nabla \cdot \boldsymbol{\theta}_{J(p+1)} = 0$ has been circumvented by numerical regularisation [18]. We use the `NGSolve` finite element library [27]–[29] for the numerical computations presented in this work.

Following the computation of $\boldsymbol{\theta}_{J(p+1)}$ for frequencies of interest between $f_{\min}$ and $f_{\max}$, the coefficients of $\mathcal{M}$ and $\mathfrak{D}$ are obtained by a simple post-processing involving integrals over B using (3) leading to the object's simulated MPT and GMPT spectral signatures. We remark that this computation could be accelerated by using a proper orthogonal decomposition (POD) based reduced order model in a similar manner to [33].

[1]We use q rather than the usual p to denote the element order avoid confusion with tensor indices

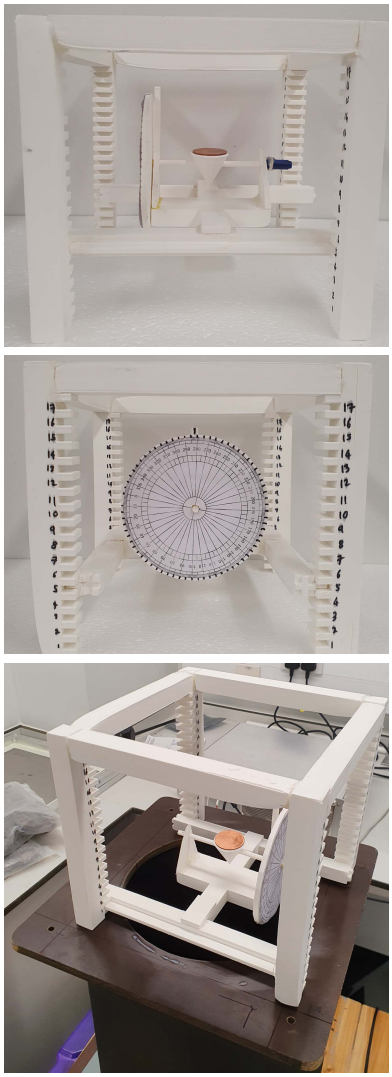

Fig. 4. Target orientation manipulator capable of rotating objects around one axis at different vertical and horizontal positions.

VII. Results

We will focus on the situation where αB is chosen to be slightly truncated copper, brass and stainless steel cones, in turn. Cones have been chosen, since, while they have a rotational and mirror symmetries, they still have non-zero rank 3 GMPT coefficients and can be used to illustrate the improvements offered over using MPTs alone for object characterisation. The sizes of each of the truncated cones are identical and have the dimensions of bottom radius 7.5 mm, top radius 0.5 mm and a height of 15 mm, hence we set $\alpha = 0.001$ m and B to be the non-dimensional truncated cone with bottom radius 7.5, top radius 0.5 and height 15. The materials of the cones are provided in Table II. While approximate measurements of the conductivity of the cones specimens have been made using a 4 terminal resistivity measurement, the reference values are still believed to be more accurate than these and, hence, have been employed in the simulations.

We have chosen the cone's canonical orientation such that the vertex of the cone is aligned with the $\boldsymbol{e}_3$ direction and the base of the cone lies in the (x_1, x_2) plane. This means that the cone has a rotational symmetry about the x_3 axis and has reflectional symmetries about the x_1 and x_2 axes. Using this information, we deduce that the 2 non-zero independent coefficients of the complex symmetric $\mathcal{M}$ are $\mathcal{M}_{11} = \mathcal{M}_{22}$ and $\mathcal{M}_{33}$ [12]. In similar way, we deduce that the 4 non-zero independent coefficients of $\mathfrak{D}$ are $\mathfrak{D}_{223} = \mathfrak{D}_{113}$, $\mathfrak{D}_{232} = \mathfrak{D}_{131}$, $\mathfrak{D}_{322} = \mathfrak{D}_{311}$ and $\mathfrak{D}_{333}$. By further noting the symmetry property (8), we find that this reduces to just 2 non-zero independent coefficients $\mathfrak{D}_{223} = \mathfrak{D}_{113} = \mathfrak{D}_{322} = \mathfrak{D}_{311}$ and $\mathfrak{D}_{333}$.

Given the reduced number of independent coefficients of $\mathcal{M}$ and $\mathfrak{D}$ for our chosen cones, placing the object on the x_3 axis and performing rotations about either the x_1, or, equivalently the x_2, axis are sufficient to determine the 2 non-zero independent coefficients of each of these tensors.

A. Copper Cone

By following the procedure described in Section V-A, we position the copper cone at $z = (0, 0, 0.15)$ m so that it lies in a uniform $\boldsymbol{H}_0^{\mathrm{Tx}}(z)$ and measure $V^{\mathrm{ind,meas}}(\theta)$ as we rotate the cone by an angle θ about the x_1 axis. We choose this position as the psuedo field generated by the receive coils (if they were used as transmit coils) is most uniform at $z = (0, 0, 0.15)$ m and $z = (0, 0, -0.15)$ m. While midpoint of the transmit coil is at $z = (0, 0, 0)$ m, the receive coils do not have sensitivity at this location, and we choose $z = (0, 0, 0.15)$ m as this easier to access than $z = (0, 0, -0.15)$ m. For further details, see Figure 6 in [25]. We set $N_\theta = 72$ and choose $\theta_n = n\Delta\theta = 2n\pi/N_\theta$ radians so that measurements are made at 5 degree increments. We use this measurement to determine $\mathcal{M}_{11} = \mathcal{M}_{22}$ and $\mathcal{M}_{33}$ for 28 frequencies between 119.25 Hz and 95 400 Hz leading to the object's measured MPT spectral signature. Then, following the measurement of the coefficients of $\mathcal{M}$, we follow the procedure in Section V-B and move the cone to $z = (0, 0, 0.343)$ m where $\boldsymbol{H}_0^{\mathrm{Tx}}(z)$ is non-uniform. Again we measure $V^{\mathrm{ind,meas}}(\theta)$ as we rotate the cone by an angle θ about the x_1 axis. We make $N_\theta = 72$ measurements and follow the procedure described in Section V-B to determine $\mathfrak{D}_{223} = \mathfrak{D}_{113} = \mathfrak{D}_{322} = \mathfrak{D}_{311}$ and $\mathfrak{D}_{333}$ for the same 28 frequencies between $f_{\min} = 119.25$ Hz and $f_{\max} = 95\,400$ Hz leading to the object's GMPT spectral signature.

To obtain the object's MPT and GMPT spectral signatures numerically, we follow the procedure in Section VI and generate a mesh of 98 419 unstructured tetrahedra to discretise the cone object B and fill the space to a truncated boundary in the form of the box $[-1000, 1000]^3$. By performing p-refinement, we find that order $q = 3$ elements lead to convergence of the tensor coefficients $\mathcal{M}_{11} = \mathcal{M}_{22}$, $\mathcal{M}_{33}$, $\mathfrak{D}_{223} = \mathfrak{D}_{113} = \mathfrak{D}_{322} = \mathfrak{D}_{311}$ and $\mathfrak{D}_{333}$ for frequencies between $f_{\min} = 119.25$ Hz and $f_{\max} = 95\,400$ Hz.

In Fig. 5, we show a comparison of the computed and measured MPT and GMPT spectral signatures where excellent agreement is observed for the computed and measured MPT spectral signatures and good agreement is observed for the computed and measured GMPT spectral signatures. The closer agreement between the spectral signatures for the simulations and measured MPT $\mathcal{M}$, compared to the GMPT $\mathfrak{D}$ is to be

TABLE II
MATERIAL PROPERTIES FOR THE COPPER, BRASS AND STAINLESS STEEL CONES

Material	μ_*	Reference σ_*(S/m)	Measured σ_*(S/m)	Simulations σ_*(S/m)
Copper	μ_0	5.95×10^7 [22]	7.63×10^7	5.95×10^7
Brass	μ_0	1.44×10^7 [24]	1.38×10^7	1.44×10^7
Stainless steel	μ_0	1.45×10^6 [8]	1.36×10^6	1.45×10^6

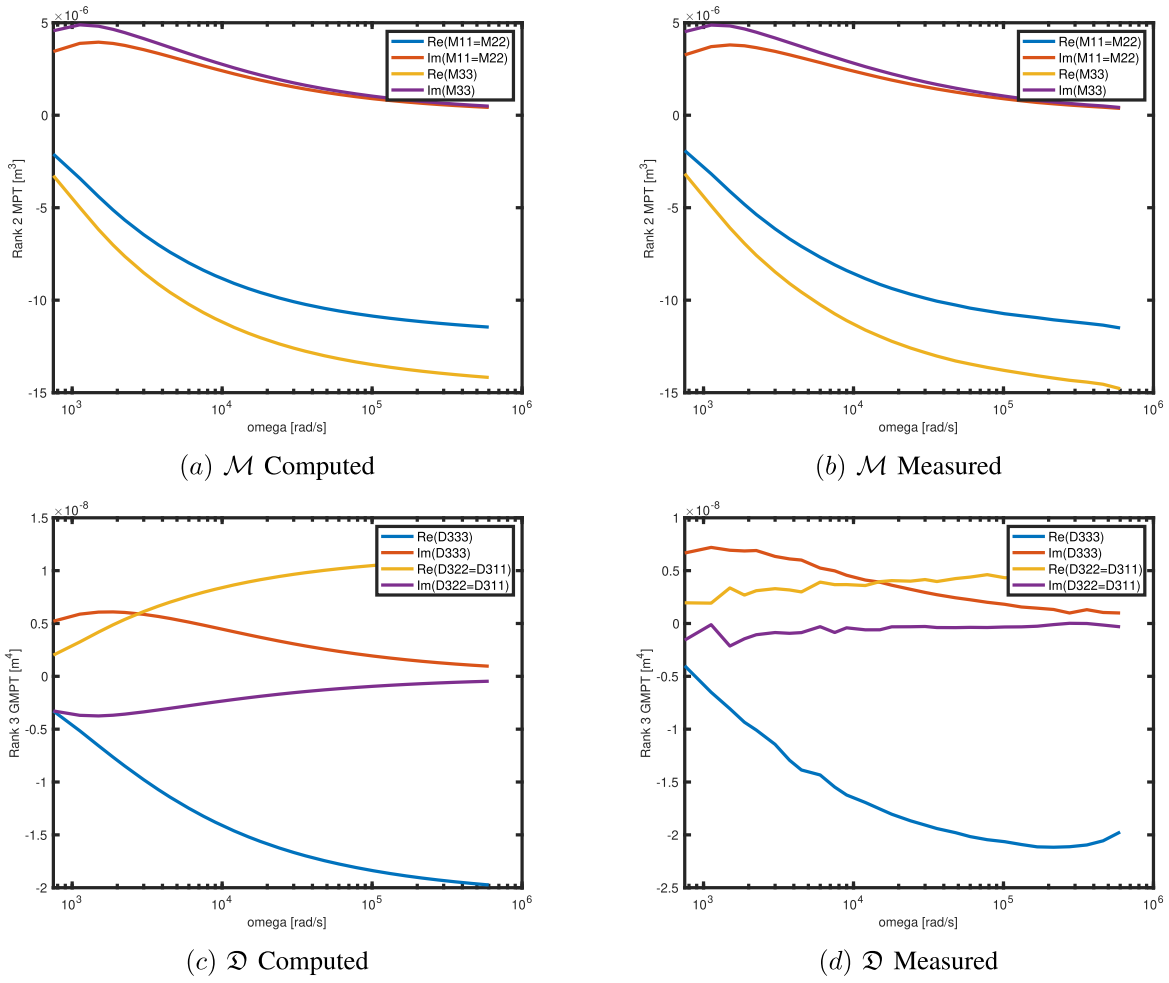

(a) $\mathcal{M}$ Computed (b) $\mathcal{M}$ Measured

(c) $\mathfrak{D}$ Computed (d) $\mathfrak{D}$ Measured

Fig. 5. Copper cone showing: spectral signature corresponding to (*a*) computed coefficients of $\boldsymbol{\mathcal{M}}$ and (*b*) measured coefficients of $\boldsymbol{\mathcal{M}}$, (*c*) computed coefficients of $\mathfrak{D}$ and (*d*) measured coefficients of $\mathfrak{D}$.

expected given that the coefficients of $\mathcal{M}$ are two orders of magnitude larger than those of $\mathfrak{D}$, which makes them easier to measure. The maximum difference between the measured and simulated $\mathcal{M}$ coefficients over the frequencies of interest is around 0.8%, which can largely be attributed to noise and measurement errors in the system with any discretisation errors being much smaller. While the shape of the GMPT spectral signatures is well captured by the measurements, the accuracy of the smaller, and harder to measure, $\mathfrak{D}$ coefficients over the frequencies of interest is lower, with differences ranging from 1% to 25% for $\mathfrak{D}_{333}$. We explain the reasons for the larger differences in Section VII-D. One noticeable difference between the simulations and measurements is the frequency at which the curves for $\mathrm{Re}(\mathfrak{D}_{322}) = \mathrm{Re}(\mathfrak{D}_{311})$ and $\mathrm{Im}(\mathfrak{D}_{333})$ cross. Even from the limited range of frequencies considered, we can see that both the real parts of the coefficients of $\mathcal{M}$ and $\mathfrak{D}$ illustrate a sigmoid behaviour with $\log\omega$ while the imaginary parts of the coefficients of $\mathcal{M}$ and $\mathfrak{D}$ have single local maxima/minima with $\log\omega$, which is reminiscent of the spectral behaviour of the MPT that has already been understood theoretically [15].

To illustrate the importance of including both the $V_2^{\mathrm{ind}}(\mathcal{M})$ and $V_3^{\mathrm{ind}}(\mathfrak{D})$ to predict V^{ind} when the object is located outside of the coil arrangement, we compare, in Fig. 6, the measured transimpedance $V^{\mathrm{ind,meas}}(\theta)$ with $V_2^{\mathrm{ind}}(\mathcal{M},\theta)$ and $V_2^{\mathrm{ind}}(\mathcal{M},\theta)+V_3^{\mathrm{ind}}(\mathfrak{D},\theta)$, each as a function of rotation angle θ about the x_1 axis, for different frequencies of excitation for an object at the position $z = (0, 0, 0.343)$ m using the simulated MPT and GMPT spectral signatures. In each case, we see the superior performance of $V_2^{\mathrm{ind}}(\mathcal{M},\theta)+V_3^{\mathrm{ind}}(\mathfrak{D},\theta)$ to predict $V^{\mathrm{ind,meas}}(\theta)$ compared to using $V_2^{\mathrm{ind}}(\mathcal{M},\theta)$ alone for an object at this position, for all frequencies considered.

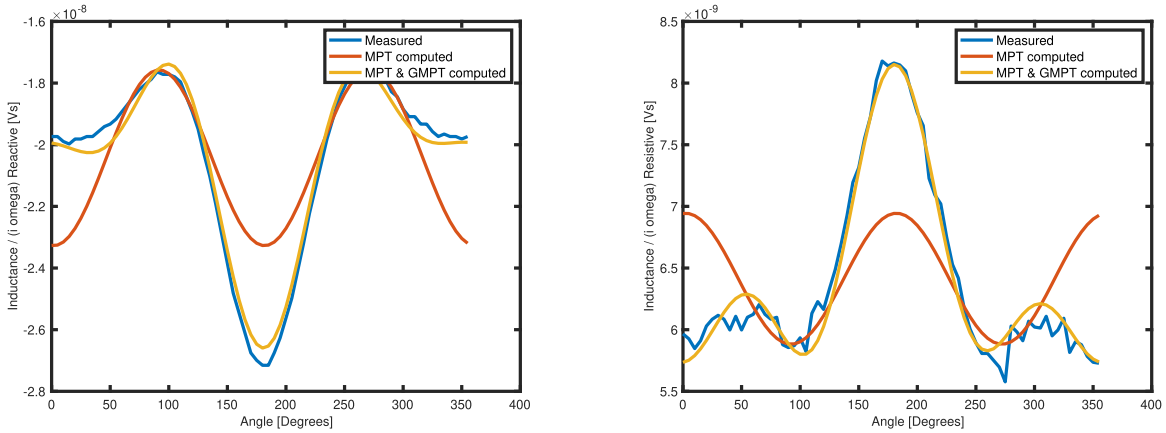

(a) f=1 193 Hz Reactive (b) f=1 193 Hz Resistive

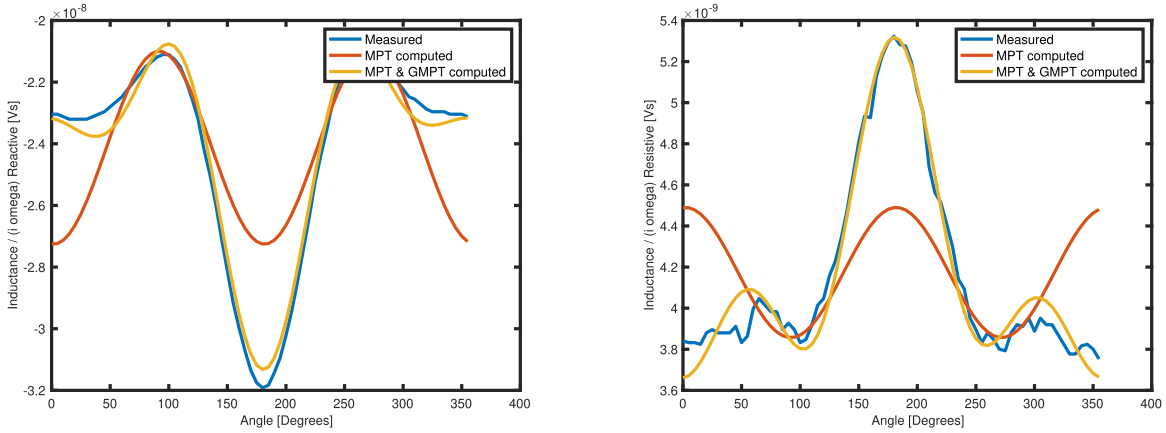

(c) f=3 816 Hz Reactive (d) f=3 816 Hz Resistive

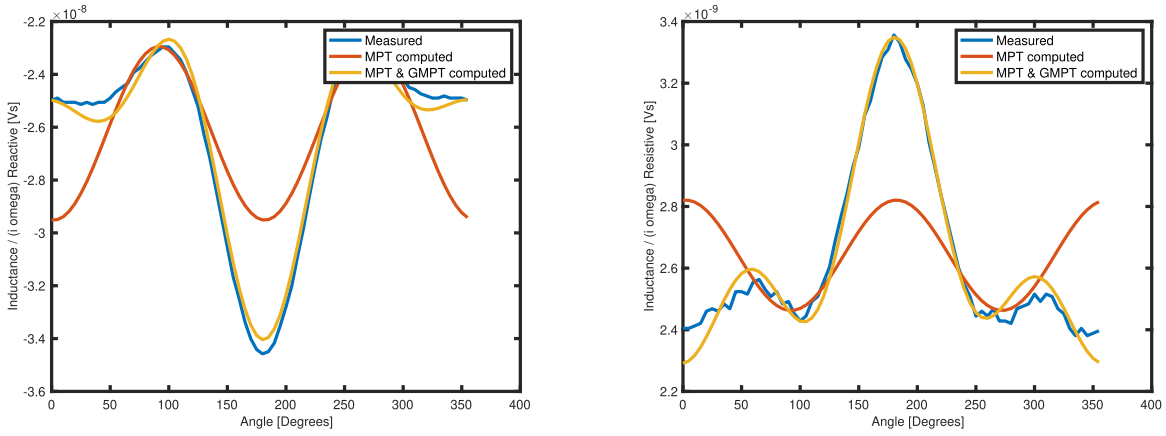

(e) f=12 402 Hz Reactive (f) f=12 402 Hz Resistive

Fig. 6. Copper cone positioned in a non-uniform field at position $\boldsymbol{z}$ = (0,0,0.343) m comparing the reactive and resistive parts of $V^{\text{ind,meas}}(\theta)$, $V_2^{\text{ind}}(\boldsymbol{\mathcal{M}}, \theta)$ and $V_2^{\text{ind}}(\boldsymbol{\mathcal{M}}, \theta) + V_3^{\text{ind}}(\mathfrak{D}, \theta)$, each normalised by ωi, showing (a) $f = 1\,193$ Hz Reactive, (b) $f = 1\,193$ Hz Resistive, (c) $f = 3\,816$ Hz Reactive, (d) $f = 3\,816$ Hz Resistive, (e) $f = 12\,402$ Hz Reactive and (f) $f = 12\,402$ Hz Resistive.

Next, we compare the performance of using the simulated and measured MPT and GMPT coefficients to predict $V^{\text{ind}}(\theta)$ at different frequencies for a cone located at $\boldsymbol{z} = (0, 0, 0.343)$ m. To do this, we compare, in Fig. 7, the reactive and resistive parts of the following residuals $V^{\text{ind, meas}}(\theta) - V_2^{\text{ind}}(\mathcal{M}, \theta)$, $V^{\text{ind, meas}}(\theta) - V_2^{\text{ind}}(\mathcal{M}^{\text{meas}}, \theta)$, $V_3^{\text{ind}}(\mathfrak{D}^{\text{meas}}, \theta)$ and $V_3^{\text{ind}}(\mathfrak{D}, \theta)$, where $\mathcal{M}$ and $\mathfrak{D}$ indicate the simulated MPT and GMPT tensors and $\mathcal{M}^{\text{meas}}$ and $\mathfrak{D}^{\text{meas}}$ the corresponding measured tensors. We observe good agreement between the different residuals indicating that using either both the simulated MPT and GMPT coefficients or both the measured MPT and GMPT coefficients provide a good prediction of $V^{\text{ind}}(\theta)$ at this location.

To confirm that $V_2^{\text{ind}}(\mathcal{M}, \theta)$ and $V_3^{\text{ind}}(\mathfrak{D}, \theta)$ do provide the dominant contributions to $V^{\text{ind,meas}}(\theta)$, and that other higher order terms do not play a significant role, we express

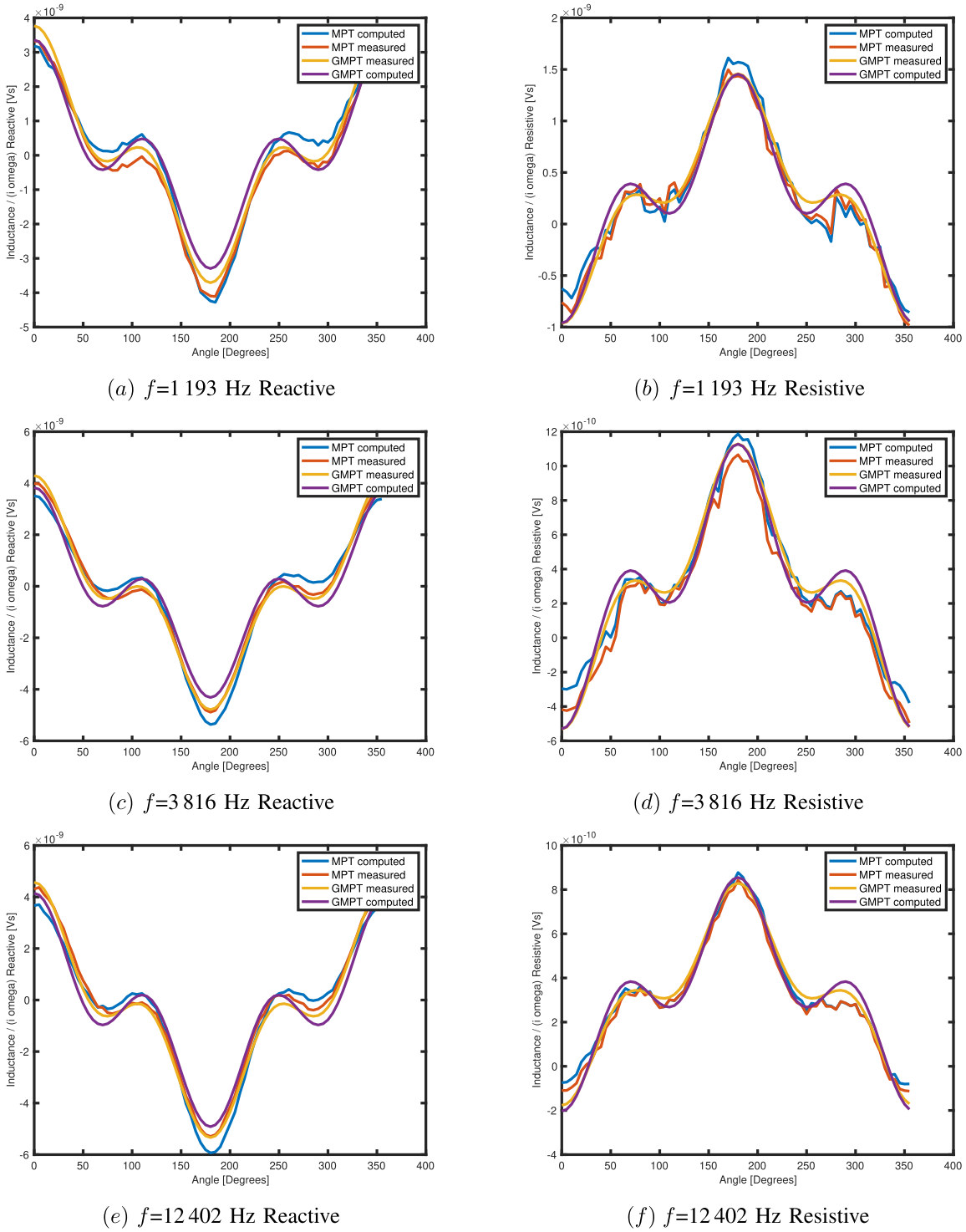

(*a*) f=1 193 Hz Reactive (*b*) f=1 193 Hz Resistive

(*c*) f=3 816 Hz Reactive (*d*) f=3 816 Hz Resistive

(*e*) f=12 402 Hz Reactive (*f*) f=12 402 Hz Resistive

Fig. 7. Copper cone positioned in a non-uniform field at position $\boldsymbol{z}$ = (0,0,0.343) m comparing the reactive and resistive parts of $V^{\text{ind, meas}}(\theta) - V_2^{\text{ind}}(\mathcal{M}, \theta)$, $V^{\text{ind, meas}}(\theta) - V_2^{\text{ind}}(\mathcal{M}^{\text{meas}}, \theta)$, $V_3^{\text{ind}}(\mathfrak{D}^{\text{meas}}, \theta)$ and $V_3^{\text{ind}}(\mathfrak{D}, \theta)$, each normalised by ωi, showing (*a*) f = 1 193 Hz Reactive, (*b*) f = 1 193 Hz Resistive, (*c*) f = 3 816 Hz Reactive, (*d*) f = 3 816 Hz Resistive, (*e*) f = 12 402 Hz Reactive and (*f*) f = 12 402 Hz Resistive.

$V^{\text{ind,meas}}(\theta)$ in the form

$$V^{\text{ind,meas}}(\theta) = \sum_{n=-K}^{K} c_n e^{in\theta},$$

and use a fast Fourier transform to determine the amplitudes $|c_n|$. Considering the products of rotation matrices in (17) that describe how the coefficients of $\mathcal{M}$ and $\mathfrak{D}$ transform under object rotation and writing powers of cosine and sine functions in terms of multiple angles, e.g. $\cos^2\theta = (1 + \cos(2\theta))/2$, $\cos^3\theta = (3\cos\theta + \cos(3\theta)/4$ and $\cos^4\theta = (3 + 4\cos(2\theta) + \cos(4\theta))/8$, we conclude that, if $V^{\text{ind,meas}}(\theta)$ can be described by a rank 2 tensor description, it will have c_n being non-zero for $n = 0, \pm 2$ while, if it additionally contains

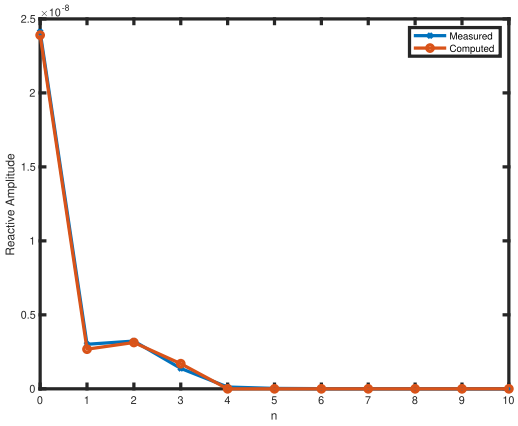

(a) Reactive

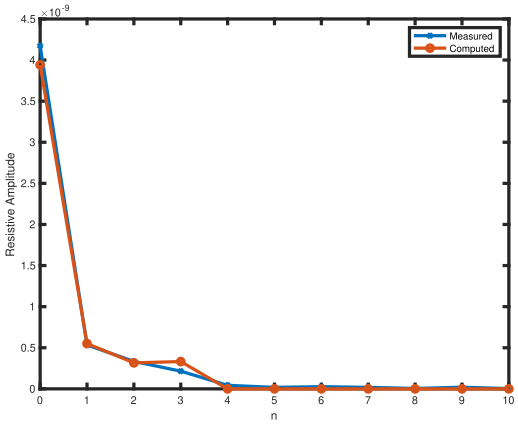

(b) Resistive

Fig. 8. Copper cone positioned in a non-uniform field at position $\boldsymbol{z}$ = (0,0,34.3) cm showing the Fourier coefficients in the expansion of the (*a*) reactive and (*b*) resistive parts of $V^{\text{ind,meas}}(\theta)$ for the case of f = 1 193 Hz.

terms associated with a rank 3 description, then, c_n for $n = \pm 1, \pm 3$ will also be non-zero. Furthermore, if $V^{\text{ind, meas}}(\theta)$ additionally contains terms associated with a rank 4 description, then, c_n for $n = \pm 4$ will also be non-zero (since in this case there would be a product of 4 rotation matrices). In Fig. 8, we show the results of applying this to the case of the cone located at $\boldsymbol{z} = (0, 0, 0.344)$ m and $f = 1\,193$ Hz and remark that the results for other locations exterior to the coil array and other frequencies are similar. We observe that $V^{\text{ind, meas}}(\theta)$ has dominant contributions associated with $n = 0, \pm 1, \pm 2, \pm 3$, which is consistent with a rank 3 tensor description being able to fully describe its behaviour. Also shown is the corresponding result for $V_2^{\text{ind}}(\mathcal{M}, \theta) + V_3^{\text{ind}}(\mathfrak{D}, \theta)$, which also has dominant contributions associated with $n = 0, \pm 1, \pm 2, \pm 3$, as expected.

To illustrate the importance of including both the $V_2^{\text{ind}}(\mathcal{M})$ and $V_3^{\text{ind}}(\mathfrak{D})$ to predict V^{ind} at different object locations, we compare, in Fig. 9, the measured transimpedance $V^{\text{ind,meas}}(\theta)$ with $V_2^{\text{ind}}(\mathcal{M}, \theta)$ and $V_2^{\text{ind}}(\mathcal{M}, \theta) + V_3^{\text{ind}}(\mathfrak{D}, \theta)$, each as a function of rotation angle θ about the x_1 axis, for different object locations and a fixed frequency of $f = 3\,816$ Hz using the simulated MPT and GMPT spectral signatures. As previously observed for the fixed position of in $\boldsymbol{z} = (0, 0, 0.343)$ m in Fig. 6, we see that including the term $V_3^{\text{ind}}(\mathfrak{D}, \theta)$ is important to accurately predict V^{ind} at different object locations. Note the results presented in Fig. 9 use a larger angle increment of $\Delta\theta = 2\pi/24$ radians, corresponding to 15 degrees, compared to those presented in Fig. 6 in order to reduce the cost of the measurements and, hence, the curves appear less smooth than before, but the conclusion remains unchanged. In a similar manner to Fig. 7, we show in Fig. 10 the corresponding transimpedence residuals for different object locations where we once again observe good agreement between the residual predicted by the simulated and measured MPT and GMPT coefficients.

Further to the results shown in Fig. 9 and 10, the accuracies according to the error measures

$$e_2^{\text{reactive}}(\mathcal{M}) = \frac{\|\text{Re}(V^{\text{ind,meas}}(\theta) - V_2^{\text{ind}}(\mathcal{M}, \theta))\|_{L^2(\theta)}}{\|\text{Re}(V^{\text{ind,meas}}(\theta)\|_{L^2(\theta)}}, \tag{20a}$$

$$e_2^{\text{resistive}}(\mathcal{M}) = \frac{\|\text{Im}(V^{\text{ind,meas}}(\theta) - V_2^{\text{ind}}(\mathcal{M}, \theta))\|_{L^2(\theta)}}{\|\text{Im}(V^{\text{ind,meas}}(\theta)\|_{L^2(\theta)}}, \tag{20b}$$

$$e_3^{\text{reactive}}(\mathcal{M}, \mathfrak{D}) = \frac{\|\text{Re}(V^{\text{ind,meas}}(\theta) - V_2^{\text{ind}}(\mathcal{M}, \theta) - V_3^{\text{ind}}(\mathfrak{D}, \theta))\|_{L^2(\theta)}}{\|\text{Re}(V^{\text{ind,meas}}(\theta)\|_{L^2(\theta)}}, \tag{20c}$$

$$e_3^{\text{resistive}}(\mathcal{M}, \mathfrak{D}) = \frac{\|\text{Im}(V^{\text{ind,meas}}(\theta) - V_2^{\text{ind}}(\mathcal{M}, \theta) - V_3^{\text{ind}}(\mathfrak{D}, \theta))\|_{L^2(\theta)}}{\|\text{Im}(V^{\text{ind,meas}}(\theta)\|_{L^2(\theta)}}, \tag{20d}$$

for a fixed frequency of $f = 3\,816$ Hz and the copper cone at different positions according to the simulated and measured coefficients of $\mathcal{M}$ and $\mathfrak{D}$ are shown in Tables III and IV, respectively. These indicate that the accuracy of the transimpedance is improved from around 10% when only the MPT is used to around 2% when either the simulated or measured GMPTs are included for all object locations considered. We have seen that $\mathfrak{D}$ can be obtained from the measurements $V^{\text{ind,meas}}(\theta)$ if the object is placed in the non-uniform field and including $V_3^{\text{ind}}(\mathfrak{D})$ is important whenever $\boldsymbol{H}_0$ is non-uniform. Importantly, as remarked in Section III, $\mathfrak{D}$ provides additional complex coefficients as a function of frequency in addition to those in $\mathcal{M}$ that can aid with object discrimination when performing object classification. Next we consider a brass and then a steel cone.

B. Brass Cone

We repeat the procedures described in Section V-A to measure $\mathcal{M}_{11} = \mathcal{M}_{22}$ and $\mathcal{M}_{33}$ at 28 frequencies between $f_{\min} = 119.25$ Hz and $f_{\max} = 95\,400$ Hz leading to the brass cone's measured MPT spectral signature. Then, we repeat the procedure in Section V-B to measure $\mathfrak{D}_{223} = \mathfrak{D}_{113} = \mathfrak{D}_{322} = \mathfrak{D}_{311}$ and $\mathfrak{D}_{333}$ for the same 28 frequencies between $f_{\min} = 119.25$ Hz and $f_{\max} = 95\,400$ Hz leading to the

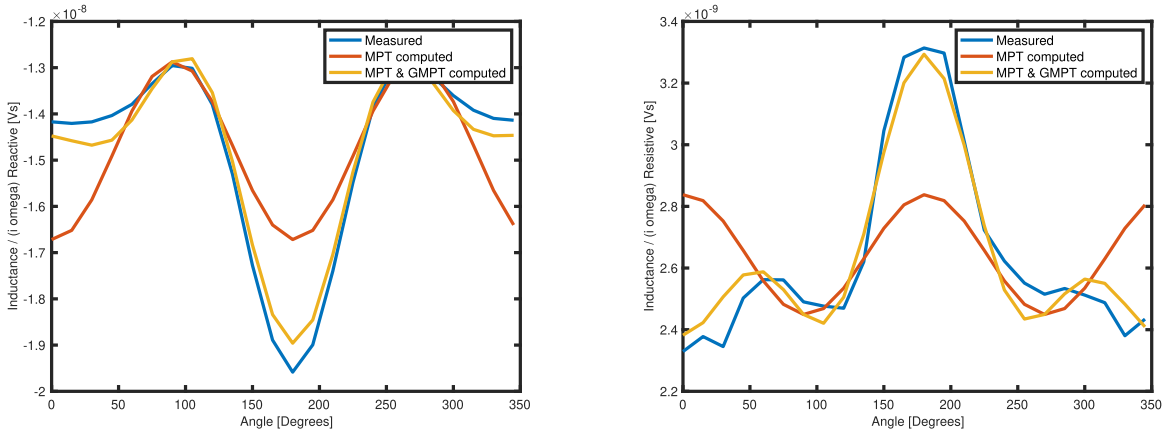

(a) $\boldsymbol{z} = (0, 0, 0.365)$ m Reactive (b) $\boldsymbol{z} = (0, 0, 0.365)$ m Resistive

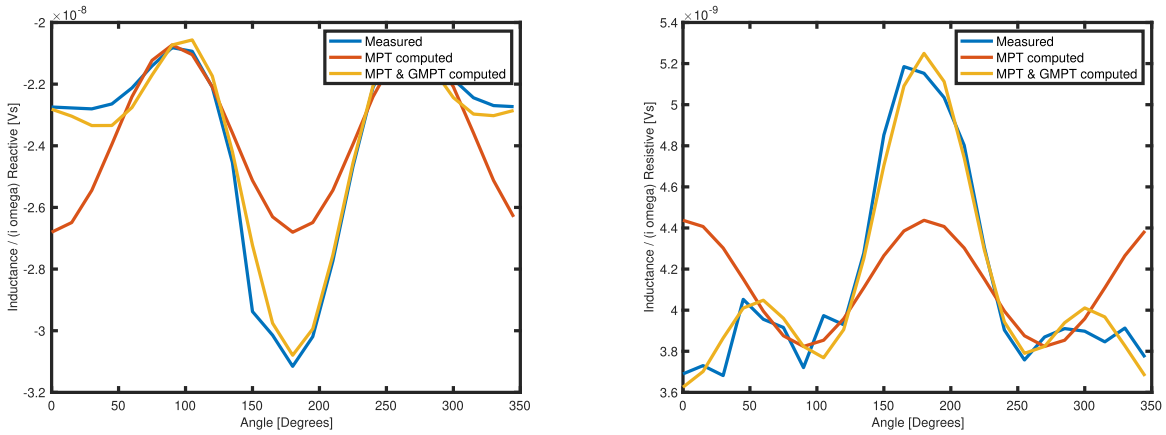

(c) $\boldsymbol{z} = (0.02, 0, 0.343)$ m Reactive (d) $\boldsymbol{z} = (0.02, 0, 0.343)$ m Resistive

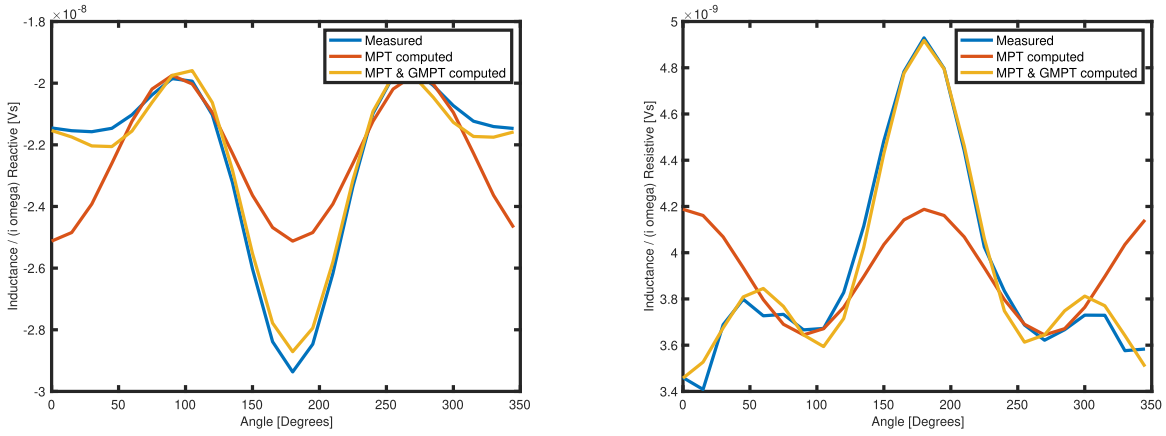

(e) $\boldsymbol{z} = (0.04, 0, 0.343)$ m Reactive (f) $\boldsymbol{z} = (0.04, 0, 0.343)$ m Resistive

Fig. 9. Copper cone positioned in a non-uniform field comparing the reactive and resistive parts of $V^{\text{ind,meas}}(\theta)$, $V_2^{\text{ind}}(\boldsymbol{\mathcal{M}}, \theta)$ and $V_2^{\text{ind}}(\boldsymbol{\mathcal{M}}, \theta) + V_3^{\text{ind}}(\mathfrak{D}, \theta)$, each normalised by ωi, for a fixed frequency of $f = 3816$ Hz showing *(a)* z = (0,0,0.365) m Reactive, *(b)* $\boldsymbol{z}$ = (0,0,0.365) m Resistive, *(c)* $\boldsymbol{z}$ = (0.02,0,0.343) m Reactive, *(d)* $\boldsymbol{z}$ = (0.02,0,0.343) m Resistive, *(e)* $\boldsymbol{z}$ = (0.04,0,0.343) m Reactive and *(f)* z = (0.04,0,0.343) m Resistive.

brass cone's measured GMPT spectral signature. To obtain the object's MPT and GMPT spectral signatures numerically, we follow the procedure in Section VI and employ the same discretisation used previously for the copper cone to simulate the coefficients $\mathcal{M}_{11} = \mathcal{M}_{22}$, $\mathcal{M}_{33}$, $\mathfrak{D}_{223} = \mathfrak{D}_{113} = \mathfrak{D}_{322} = \mathfrak{D}_{311}$ and $\mathfrak{D}_{333}$ for frequencies between $f_{\min} = 119.25$ Hz and $f_{\max} = 95\,400$ Hz for the brass cone.

In Fig. 11, we show a comparison of the computed and measured MPT and GMPT spectral signatures for the brass cone where excellent agreement is observed for the computed and measured MPT spectral signatures and good agreement is observed for the computed and measured GMPT spectral signatures. Again note that the non-zero independent coefficients of $\mathfrak{D}$ are 2 orders of magnitude smaller than those of

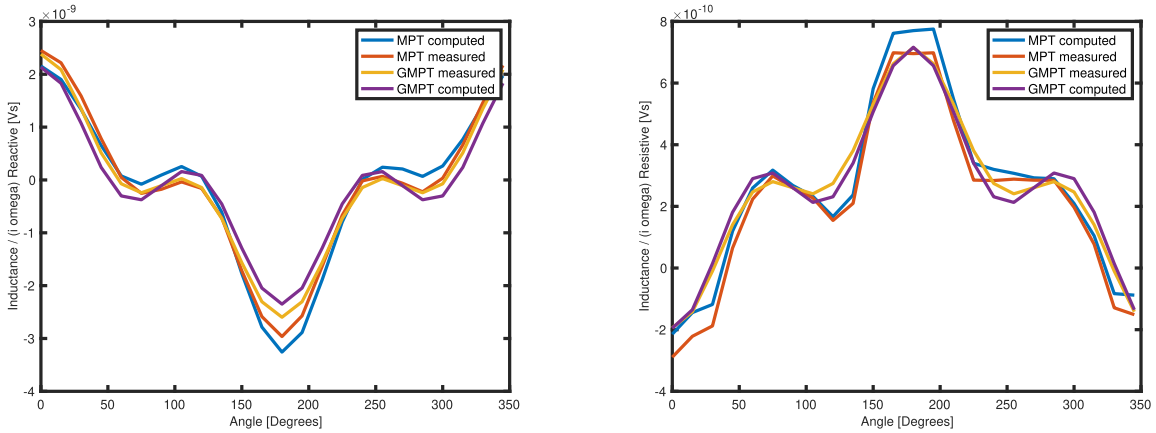

(a) $\boldsymbol{z} = (0, 0, 0.365)$ m Reactive

(b) $\boldsymbol{z} = (0, 0, 0.365)$ m Resistive

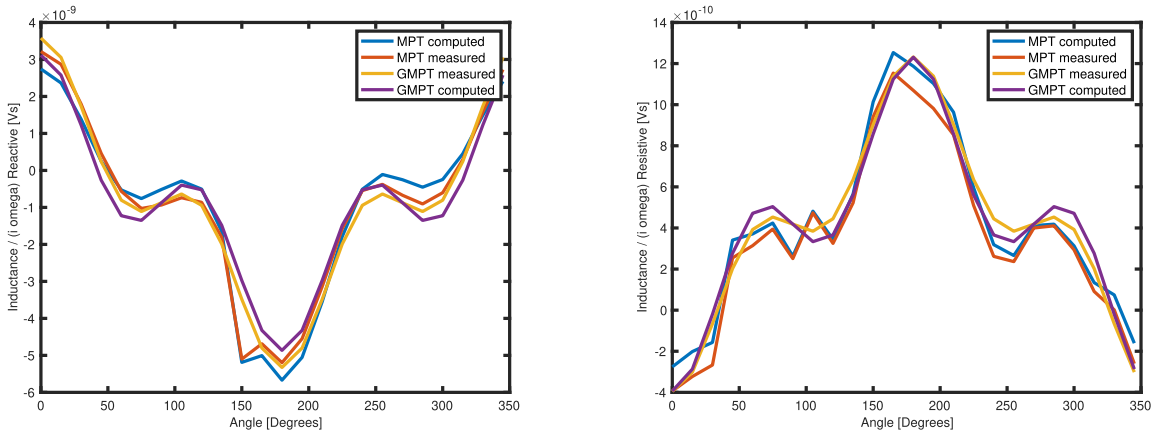

(c) $\boldsymbol{z} = (0.02, 0, 0.343)$ m Reactive

(d) $\boldsymbol{z} = (0.02, 0, 0.343)$ m Resistive

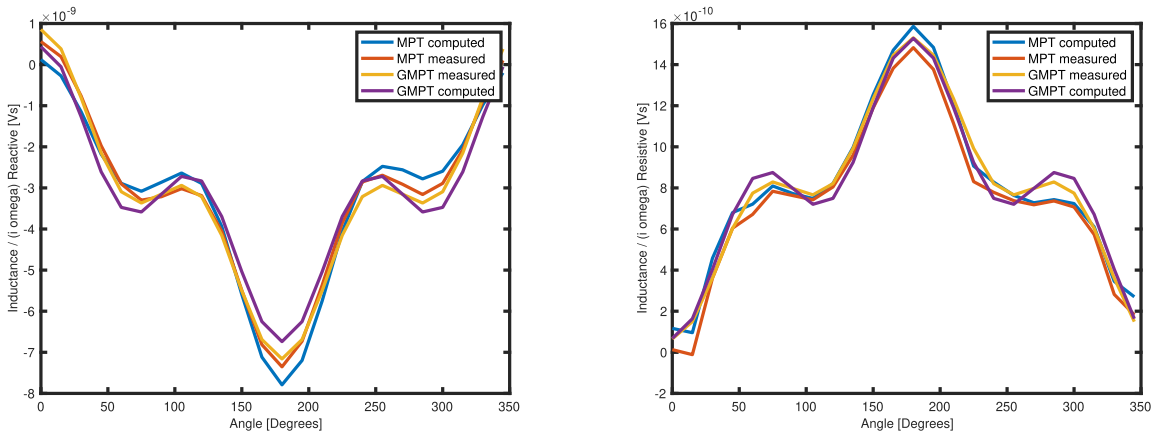

(e) $\boldsymbol{z} = (0.04, 0, 0.343)$ m Reactive

(f) $\boldsymbol{z} = (0.04, 0, 0.343)$ m Resistive

Fig. 10. Copper cone positioned in a non-uniform field comparing the reactive and resistive parts of $V^{\text{ind,meas}} - V_2^{\text{ind}}(\mathcal{M})$, $V^{\text{ind,meas}} - V_2^{\text{ind}}(\mathcal{M}^{\text{meas}})$, $V_3^{\text{ind}}(\mathfrak{D}^{\text{meas}})$ and $V_3^{\text{ind}}(\mathfrak{D})$, each normalised by ωi, for a fixed frequency of f = 3816 Hz showing *(a)* $\boldsymbol{z}$ = (0,0,0.365) m Reactive, *(b)* $\boldsymbol{z}$ = (0,0,0.365) m Resistive, *(c)* $\boldsymbol{z}$ = (0.02,0,0.343) m Reactive, *(d)* $\boldsymbol{z}$ = (0.02,0,0.343) m Resistive, *(e)* $\boldsymbol{z}$ = (0.04,0,0.343) m Reactive and *(f)* $\boldsymbol{z}$ = (0.04,0,0.343) m Resistive.

$\mathcal{M}$ and, hence, we should not expect them to be measured as accurately as those of $\mathcal{M}$, with the difference between the measured and computed MPT and GMPTs being similar to those for the copper cone. A similar noticeable difference between the simulations and measurements to the copper cone is the frequency at which the curves for $\text{Re}(\mathfrak{D}_{322}) = \text{Re}(\mathfrak{D}_{311})$ and $\text{Im}(\mathfrak{D}_{311})$ cross. Also, in a similar manner to Fig. 5, we observe that the coefficients of both the real parts of the coefficients of $\mathcal{M}$ and $\mathfrak{D}$ show a sigmoid behaviour with $\log \omega$ while the coefficients of the imaginary parts of the coefficients of $\mathcal{M}$ and $\mathfrak{D}$ have single local maxima/minima with $\log \omega$.

Comparable curves to those produced in Fig. 6-10 have also been found for the brass cone and similar agreements can be drawn for this object. Hence, we only provide the tabular

TABLE III
COPPER CONE POSITIONED IN A NON-UNIFORM FIELD COMPARING THE ERROR MEASURES DEFINED IN (20) FOR COMPUTED $\mathcal{M}$ AND $\mathfrak{D}$ TENSORS, A FIXED FREQUENCY OF $f = 3\,816$ HZ AND DIFFERENT OBJECT LOCATIONS

z (m)	$e_2^{\text{reactive}}(\mathcal{M})$	$e_2^{\text{resistive}}(\mathcal{M})$	$e_3^{\text{reactive}}(\mathcal{M},\mathfrak{D})$	$e_3^{\text{resistive}}(\mathcal{M},\mathfrak{D})$
(0,0,0.343)	0.096309	0.097819	0.017664	0.021213
(0,0,0.365)	0.096627	0.103190	0.023734	0.026163
(0,0,0.382)	0.092338	0.090466	0.025041	0.021797
(0.02,0,0.343)	0.097654	0.101031	0.023663	0.022160
(0.04,0,0.343)	0.092492	0.098122	0.017634	0.016462

TABLE IV
COPPER CONE POSITIONED IN A NON-UNIFORM FIELD COMPARING THE ERROR MEASURES DEFINED IN (20) FOR MEASURED $\mathcal{M}$ AND $\mathfrak{D}$ TENSORS, A FIXED FREQUENCY OF $f = 3\,816$ HZ AND DIFFERENT OBJECT LOCATIONS

z	$e_2^{\text{reactive}}(\mathcal{M}^{\text{meas}})$	$e_2^{\text{resistive}}(\mathcal{M}^{\text{meas}})$	$e_3^{\text{reactive}}(\mathcal{M}^{\text{meas}},\mathfrak{D}^{\text{meas}})$	$e_3^{\text{resistive}}(\mathcal{M}^{\text{meas}},\mathfrak{D}^{\text{meas}})$
0,0,0.343)	0.097677	0.12152	0.017625	0.020402
(0,0,0.365)	0.097935	0.14225	0.018959	0.023640
(0,0,0.382)	0.093599	0.16891	0.020277	0.021123
(0.02,0,0.343)	0.098964	0.14300	0.023077	0.022878
(0.04,0,0.343)	0.093994	0.22635	0.018504	0.013540

TABLE V
BRASS CONE POSITIONED IN A NON-UNIFORM FIELD COMPARING THE ERROR MEASURES DEFINED IN (20) FOR COMPUTED $\mathcal{M}$ AND $\mathfrak{D}$ TENSORS, A FIXED FREQUENCY OF $f = 3\,816$ HZ AND DIFFERENT OBJECT LOCATIONS

z	$e_2^{\text{reactive}}(\mathcal{M})$	$e_2^{\text{resistive}}(\mathcal{M})$	$e_3^{\text{reactive}}(\mathcal{M},\mathfrak{D})$	$e_3^{\text{resistive}}(\mathcal{M},\mathfrak{D})$
(0,0,0.343)	0.113650	0.104790	0.047887	0.023568
(0,0,0.361)	0.108850	0.102740	0.042399	0.026610
(0,0,0.381)	0.094877	0.090336	0.031265	0.023487
(0.02,0,0.341)	0.094400	0.101360	0.025379	0.019437
(0.04,0,0.336)	0.103850	0.102580	0.027634	0.020289

TABLE VI
BRASS CONE POSITIONED IN A NON-UNIFORM FIELD COMPARING THE ERROR MEASURES DEFINED IN (20) FOR MEASURED $\mathcal{M}$ AND $\mathfrak{D}$ TENSORS, A FIXED FREQUENCY OF $f = 3\,816$ HZ AND DIFFERENT OBJECT LOCATIONS

z	$e_2^{\text{reactive}}(\mathcal{M}^{\text{meas}})$	$e_2^{\text{resistive}}(\mathcal{M}^{\text{meas}})$	$e_3^{\text{reactive}}(\mathcal{M}^{\text{meas}},\mathfrak{D}^{\text{meas}})$	$e_3^{\text{resistive}}(\mathcal{M}^{\text{meas}},\mathfrak{D}^{\text{meas}})$
(0,0,0.343)	0.113610	0.117590	0.040301	0.021583
(0,0,0.361)	0.111670	0.120900	0.036134	0.024457
(0,0,0.381)	0.096422	0.120910	0.022136	0.016521
(0.02,0,0.341)	0.096394	0.113750	0.035334	0.020949
(0.04,0,0.336)	0.104000	0.115820	0.033121	0.023151

summaries in Tables V and VI, which illustrate comparable accuracies for the simulated and measured coefficients of $\mathcal{M}$ and $\mathfrak{D}$ for the brass cone positioned at different locations compared to those shown in Tables III and IV.

C. Steel Cone

We repeat the procedures described in Section V-A to measure $\mathcal{M}_{11} = \mathcal{M}_{22}$ and $\mathcal{M}_{33}$ at 28 frequencies between $f_{\min} = 119.25$ Hz and $f_{\max} = 95\,400$ Hz leading to the steel cone's measured MPT spectral signature. Then, we repeat the procedure in Section V-B to measure $\mathfrak{D}_{223} = \mathfrak{D}_{113} = \mathfrak{D}_{322} = \mathfrak{D}_{311}$ and $\mathfrak{D}_{333}$ for the same 28 frequencies between $f_{\min} = 119.25$ Hz and $f_{\max} = 95\,400$ Hz leading to the steel cone's measured GMPT spectral signature. To obtain the object's MPT and GMPT spectral signatures numerically we the employ the same discretisation as before and repeat the process described for the copper and brass cones.

In Fig. 12 we show a comparison of the computed and measured MPT and GMPT spectral signatures for the steel cone where excellent agreement is observed for the computed and measured MPT spectral signatures and good agreement is observed for the computed and measured GMPT spectral signatures Again note that the non-zero independent coefficients of $\mathfrak{D}$ are 2 orders of magnitude smaller than those of $\mathcal{M}$ and, hence, we should not expect them to be measured as accurately as those of $\mathcal{M}$, in this case the minimum difference between the measured and computed MPT coefficients is much less than 1% and the minimum differences between measurement and simulations for $\mathfrak{D}_{333}$ is 5% while for $\mathfrak{D}_{322}$ it is 9.7%. In a similar manner to Fig. 5 and 11, we can see that the coefficients of both the real parts of $\mathcal{M}$ and $\mathfrak{D}$ illustrate a sigmoid behaviour with $\log\omega$ while the coefficients of the imaginary parts of $\mathcal{M}$ and $\mathfrak{D}$ have single local maxima/minima with $\log\omega$.

In a similar manner to the brass cone, we only provide the tabular summaries in Tables VII and VIII, which illustrate comparable accuracies for the simulated and measured coefficients of $\mathcal{M}$ and $\mathfrak{D}$ for the steel cone positioned at different locations.

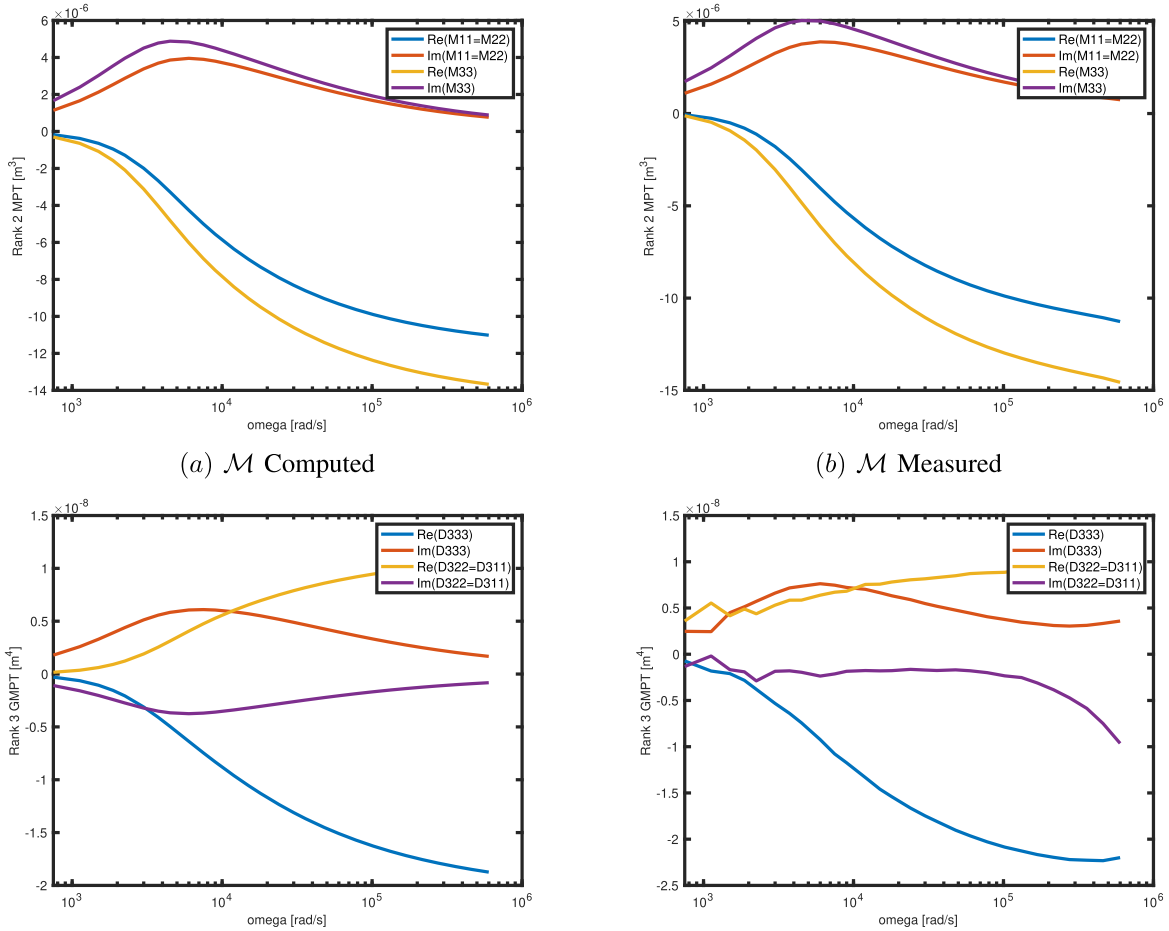

(a) $\mathcal{M}$ Computed (b) $\mathcal{M}$ Measured

(c) $\mathfrak{D}$ Computed (d) $\mathfrak{D}$ Measured

Fig. 11. Brass cone showing: spectral signatures corresponding to (*a*) computed coefficients of $\mathcal{M}$ and (*b*) measured coefficients of $\mathcal{M}$, (*c*) computed coefficients of $\mathfrak{D}$ and (*d*) measured coefficients of $\mathfrak{D}$.

TABLE VII

STEEL CONE POSITIONED IN A NON-UNIFORM FIELD COMPARING THE ERROR MEASURES DEFINED IN (20) FOR COMPUTED $\mathcal{M}$ AND $\mathfrak{D}$ TENSORS, A FIXED FREQUENCY OF $f = 3816$ HZ AND DIFFERENT OBJECT LOCATIONS

z	$e_2^{\text{reactive}}(\mathcal{M})$	$e_2^{\text{resistive}}(\mathcal{M})$	$e_3^{\text{reactive}}(\mathcal{M},\mathfrak{D})$	$e_3^{\text{resistive}}(\mathcal{M},\mathfrak{D})$
(0,0,34.3)	0.096921	0.092994	0.024522	0.021665
(0,0,36.1)	0.095550	0.089722	0.030501	0.027052
(0,0,38.1)	0.099927	0.085682	0.052521	0.033339
(2,0,34.1)	0.103670	0.090383	0.056694	0.022046
(4,0,33.7)	0.097569	0.093506	0.024934	0.023298

TABLE VIII

STEEL CONE POSITIONED IN A NON-UNIFORM FIELD COMPARING THE ERROR MEASURES DEFINED IN (20) FOR MEASURED $\mathcal{M}$ AND $\mathfrak{D}$ TENSORS, A FIXED FREQUENCY OF $f = 3816$ HZ AND DIFFERENT OBJECT LOCATIONS

z	$e_2^{\text{reactive}}(\mathcal{M}^{\text{meas}})$	$e_2^{\text{resistive}}(\mathcal{M}^{\text{meas}})$	$e_3^{\text{reactive}}(\mathcal{M}^{\text{meas}},\mathfrak{D}^{\text{meas}})$	$e_3^{\text{resistive}}(\mathcal{M}^{\text{meas}},\mathfrak{D}^{\text{meas}})$
(0,0,34.3)	0.097585	0.100140	0.019174	0.031757
(0,0,36.1)	0.095101	0.102820	0.012218	0.029557
(0,0,38.1)	0.100400	0.100500	0.046089	0.032477
(2,0,34.1)	0.103190	0.096255	0.056485	0.030406
(4,0,33.7)	0.097142	0.097605	0.024977	0.022437

D. Accuracy of MPT and GMPT Measurements

The high level of accuracy in the measured MPT coefficients has been achieved as the multi-coil arrangement was originally designed and built to characterise objects by their rank 2 MPTs. The design, experimental repeatability and accuracy of the system has been reported in [25]. In this work, we have extended our original measurement system to allow, for the first time, the measurement of the rank 3 GMPT

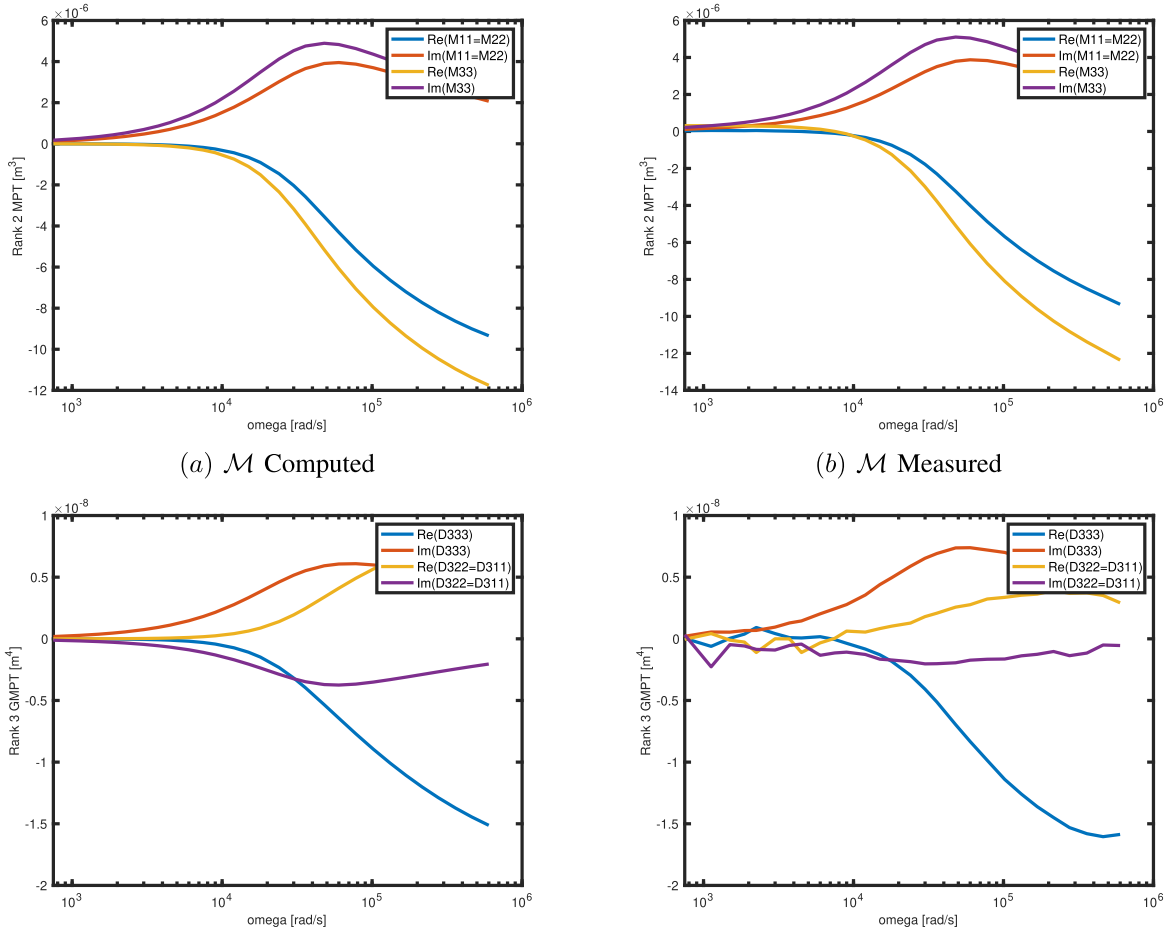

(a) $\mathcal{M}$ Computed

(b) $\mathcal{M}$ Measured

(c) $\mathfrak{D}$ Computed

(d) $\mathfrak{D}$ Measured

Fig. 12. Steel cone showing: (*a*) computed coefficients of $\mathcal{M}$ and (*b*) measured coefficients of $\mathcal{M}$, (*c*) computed coefficients of $\mathfrak{D}$ and (*d*) measured coefficients of $\mathfrak{D}$.

coefficients by placing the object in the non-uniform $\boldsymbol{H}_0$ field outside of the bore of the coil arrangement. There are several potential sources of error in the GMPT measurements. Firstly, the bore of the measurement apparatus is electrostatically shielded to remove any capacitive coupling of a target object to the coils. However, this is not the case when the target object is placed outside of the bore where $\boldsymbol{H}_0$ is non-uniform. This is further complicated when the object is rotated as the capacitive coupling may be different for different orientations. This results in experimental error that is observed in the higher frequencies in the measured spectrum. Secondly, the measurement system was designed to be sensitive across the bore where $\boldsymbol{H}_0$ is uniform, which means high signal-to-noise ratio (SNR) in this area. However, the SNR starts to get smaller as the target object moves away from where $\boldsymbol{H}_0(z)$ is uniform. This means there may be errors in the experimental results introduced by measurement noise. Thirdly, the apparatus was built to ensure a precise position and orientation manipulation, these manipulations will contain inaccuracies, which result in differences in $\boldsymbol{H}_0(z)$ as well as the rotational configuration of the object compared to the analytical model. Moreover, any small imperfections of the coils, which do not affect rank 2 MPT characterisation results in the uniform field, may become more apparent in measurements outside of this region. Fourthly, a four-wire resistivity measurement was used to characterise resistivity of the cones. However, these may have small errors in the results meaning the materials modelled may be slightly different in simulations. While these sources of errors are not significant individually, the smaller rank 3 GMPT coefficients and the cumulative sum of these errors, leads to greater inaccuracies in their measurement when compared to those of the MPT. To improve the accuracy of GMPTs significantly would require the design of a new coil arrangement that is optimised to produce non-uniform $\boldsymbol{H}_0$ fields, which can be predicted with a high level of accuracy, and address the points raised above.

VIII. Conclusion

In this work we have explained the limitations of using an MPT spectral signature alone to characterise objects since the object is then characterised by just 6 complex coefficients as a function of ω. For objects with rotational and/or reflectional symmetries the number of independent coefficients is much fewer and this makes it difficult to discriminate between objects in object classification and to determine which way an object is pointing. Using GMPTs provides additional complex

coefficients as a function of ω, which can aid with discriminating between objects and, hence, they have the potential to improve classification. We have shown, for the first time, that GMPT coefficients and their spectral signature can be obtained in practice from measurements of $(\boldsymbol{H}_\alpha - \boldsymbol{H}_0)(\boldsymbol{x})$ from a coil arrangement. The resulting measured GMPT spectral signature we have obtained are in good agreement with the simulated GMPT spectral signatures we found from numerical simulations using finite elements, while the larger measured MPTs that exhibit a very high level of accuracy. We have illustrated that including the GMPT object characterisation information is important to accurately predict $(\boldsymbol{H}_\alpha - \boldsymbol{H}_0)(\boldsymbol{x})$ whenever the background field is non-uniform for a sequence of copper, brass and steel cones placed at different locations. Our future work includes designing and building a new measurement system that can achieve greater accuracy of GMPT coefficients.

In this work, we have limited consideration to objects with $\mu_* = \mu_0$ and to the cone geometry. For magnetic objects, $\mathfrak{N}$ can not be neglected and includes important characterisation information. Furthermore, many practical objects have fewer (or no) symmetries compared to the cone, which increases the number of MPT and GMPT coefficients needed to characterise the object. The effect of an object's symmetry group on GMPT coefficients will be the subject of a forthcoming work.

REFERENCES

[1] O. A. Abdel-Rehim, J. L. Davidson, L. A. Marsh, M. D. O'Toole, and A. J. Peyton, "Magnetic polarizability tensor spectroscopy for low metal anti-personnel mine surrogates," *IEEE Sensors J.*, vol. 16, no. 10, pp. 3775–3783, May 2016.

[2] D. Ambruš, D. Vasić, and V. Bilas, "Robust estimation of metal target shape using time-domain electromagnetic induction data," *IEEE Trans. Instrum. Meas.*, vol. 65, no. 4, pp. 795–807, Apr. 2016.

[3] H. Ammari, A. Buffa, and J. C. Nédélec, "A justification of eddy currents model for the Maxwell equations," *SIAM J. Appl. Math.*, vol. 60, no. 5, pp. 1805–1823, 2000.

[4] H. Ammari, J. Chen, Z. Chen, J. Garnier, and D. Volkov, "Target detection and characterization from electromagnetic induction data," *J. Math. Pures Appl.*, vol. 101, no. 1, pp. 54–75, Jan. 2014.

[5] H. Ammari, J. Chen, Z. Chen, D. Volkov, and H. Wang, "Detection and classification from electromagnetic induction data," *J. Comput. Phys.*, vol. 301, pp. 201–217, Nov. 2015.

[6] H. Ammari and H. Kang, *Polarization and Moment Tensors with Applications to Inverse Problems and Effective Medium Theory*. New York, NY, USA: Springer-Verlag, 2007.

[7] E. E. Callaghan and S. H. Maslen, "The magnetic field of a finite solenoid," NASA, Washington, DC, USA, Tech. Note D-465, 1960.

[8] Wikipedia Contributors. *Electrical Resistivity and Conductivity, Wikipedia, The Free Encyclopedia*. Accessed: Jun. 25, 2021. [Online]. Available: https://en.wikipedia.org/wiki/Electrical_resistivity_and_conductivity

[9] J. L. Davidson, O. A. Abdel-Rehim, P. Hu, L. A. Marsh, M. D. O'Toole, and A. J. Peyton, "On the magnetic polarizability tensor of U.S. Coinage," *Meas. Sci. Technol.*, vol. 29, no. 3, Mar. 2018, Art. no. 035501.

[10] B. Dekdouk, C. Ktistis, L. A. Marsh, D. W. Armitage, and A. J. Peyton, "Towards metal detection and identification for humanitarian demining using magnetic polarizability tensor spectroscopy," *Meas. Sci. Technol.*, vol. 26, no. 11, 2015, Art. no. 115501.

[11] N. Karimian, M. D. O'Toole, and A. J. Peyton, "Electromagnetic tensor spectroscopy for sorting of shredded metallic scrap," in *Proc. IEEE SENSORS*, Oct. 2017, pp. 1–3.

[12] P. D. Ledger and W. R. B. Lionheart, "Characterizing the shape and material properties of hidden targets from magnetic induction data," *IMA J. Appl. Math.*, vol. 80, no. 6, pp. 1776–1798, 2015.

[13] P. D. Ledger and W. R. B. Lionheart, "An explicit formula for the magnetic polarizability tensor for object characterization," *IEEE Trans. Geosci. Remote Sens.*, vol. 56, no. 6, pp. 3520–3533, Jun. 2018.

[14] P. D. Ledger and W. R. B. Lionheart, "Generalised magnetic polarizability tensors," *Math. Methods Appl. Sci.*, vol. 41, no. 8, pp. 3175–3196, May 2018.

[15] P. D. Ledger and W. R. B. Lionheart, "The spectral properties of the magnetic polarizability tensor for metallic object characterisation," *Math. Methods Appl. Sci.*, vol. 43, no. 1, pp. 78–113, Jan. 2020.

[16] P. D. Ledger, W. R. B. Lionheart, and A. A. S. Amad, "Characterisation of multiple conducting permeable objects in metal detection by polarizability tensors," *Math. Methods Appl. Sci.*, vol. 42, no. 3, pp. 830–860, Dec. 2018.

[17] P. D. Ledger, B. A. Wilson, A. A. S. Amad, and W. R. B. Lionheart, "Identification of metallic objects using spectral magnetic polarizability tensor signatures: Object characterisation and invariants," *Int. J. Numer. Methods Eng.*, vol. 122, no. 15, pp. 3941–3984, Aug. 2021.

[18] P. D. Ledger and S. Zaglmayr, "*hp*-finite element simulation of three-dimensional eddy current problems on multiply connected domains," *Comput. Methods Appl. Mech. Eng.*, vol. 199, pp. 3386–3401, Dec. 2010.

[19] J. Makkonen *et al.*, "KNN classification of metallic targets using the magnetic polarizability tensor," *Meas. Sci. Technol.*, vol. 25, no. 5, 2014, Art. no. 055105.

[20] J. Makkonen *et al.*, "Improving reliability for classification of metallic objects using a WTMD portal," *Meas. Sci. Technol.*, vol. 26, no. 10, Oct. 2015, Art. no. 105103.

[21] L. A. Marsh, C. Ktistis, A. Järvi, D. W. Armitage, and A. J. Peyton, "Three-dimensional object location and inversion of the magnetic polarizability tensor at a single frequency using a walk-through metal detector," *Meas. Sci. Technol.*, vol. 24, no. 4, Apr. 2013, Art. no. 045102.

[22] C. R. Nave. *Resistivity and Temperature Coefficient at 20 Degrees C, Hyper Physics*. Accessed: Jun. 25, 2021. [Online]. Available: http://hyperphysics.phy-astr.gsu.edu/hbase/Tables/rstiv.html

[23] S. J. Norton and I. J. Won, "Identification of buried unexploded ordnance from broadband electromagnetic induction data," *IEEE Trans. Geosci. Remote Sens.*, vol. 39, no. 10, pp. 2253–2261, Oct. 2001.

[24] Electronics Notes. *Electrical Resistivity Table for Common Materials*. Accessed: Jun. 25, 2021. [Online]. Available: https://www.electronics-notes.com/articles/basic_concepts/resistance/electrical-resistivity-table-materials.php

[25] T. Ozdeger, J. L. Davidson, W. van Verre, L. A. Marsh, W. R. B. Lionheart, and A. J. Peyton, "Measuring the magnetic polarizability tensor using an axial multi-coil geometry," *IEEE Sensors J.*, vol. 21, no. 17, pp. 19322–19333, Sep. 2021.

[26] K. Schmidt, O. Sterz, and R. Hiptmair, "Estimating the eddy-current modeling error," *IEEE Trans. Magn.*, vol. 44, no. 6, pp. 686–689, Jun. 2008.

[27] J. Schöberl, "NETGEN an advancing front 2D/3D-mesh generator based on abstract rules," *Comput. Vis. Sci.*, vol. 1, no. 1, pp. 41–52, Jul. 1997.

[28] J. Schöberl, "C++11 implementation of finite elements in NGSolve," Inst. Anal. Sci. Comput., Vienna Univ. Technol., Vienna, Austria, Tech. Rep. ASC Rep. 30/2014, 2014.

[29] J. Schöberl and S. Zaglmayr, "High order Nédélec elements with local complete sequence properties," *COMPEL-Int. J. Comput. Math. Electr. Electron. Eng.*, vol. 24, no. 2, pp. 374–384, Jun. 2005.

[30] W. R. Scott and G. D. Larson, "Measured dipole expansion of discrete relaxations to represent the electromagnetic induction response of buried metal targets," in *Proc. SPIE, Detection Sensing Mines, Explosive Objects, Obscured Targets XV*, vol. 7664, FL, USA, 2010, Art. no. 76640E.

[31] W. R. Scott, "Broadband array of electromagnetic induction sensors for detecting buried landmines," in *Proc. IEEE Int. Geosci. Remote Sens. Symp. (IGARSS)*, Boston, MA, USA, Jul. 2008, pp. 375–378.

[32] W. R. Scott and M. McFadden, "Wideband measurement of the magnetic susceptibility of soils and the magnetic polarizability of metallic objects," in *Proc. IEEE Int. Geosci. Remote Sens. Symp.*, Jul. 2012, pp. 3170–3173.

[33] B. A. Wilson and P. D. Ledger, "Efficient computation of the magnetic polarizabiltiy tensor spectral signature using proper orthogonal decomposition," *Int. J. Numer. Methods Eng.*, vol. 122, no. 8, pp. 1940–1963, Apr. 2021.

[34] B. A. Wilson, P. D. Ledger, and W. R. B. Lionheart, "Identification of metallic objects using spectral magnetic polarizability tensor signatures: Object classification," 2021, *arXiv:2110.06624*.

[35] Y. Zhao, W. Yin, C. Ktistis, D. Butterworth, and A. J. Peyton, "Determining the electromagnetic polarizability tensors of metal objects during in-line scanning," *IEEE Trans. Instrum. Meas.*, vol. 65, no. 5, pp. 1172–1181, May 2016.